

Callisto's Atmosphere: The Oxygen Enigma

Shane R. Carberry Mogan¹ , Lucas Liuzzo¹ , Andrew R. Poppe¹ , Sven Simon² ,
Jamey R. Szalay³ , Orenthal J. Tucker⁴ , and Robert E. Johnson^{5,6} 

¹University of California, Berkeley, Berkeley, CA, USA, ²Georgia Institute of Technology, Atlanta, GA, USA, ³Princeton University, Princeton, NJ, USA, ⁴NASA Goddard Space Flight Center, Greenbelt, MD, USA, ⁵University of Virginia, Charlottesville, VA, USA, ⁶New York University, New York, NY, USA

Key Points:

- We estimate the energy deposited by the thermal and energetic components of the Jovian magnetospheric plasma in Callisto's atmosphere
- We calculate O₂ column densities in Callisto's atmosphere corresponding to the energies of the plasma fluxes impacting the surface
- Radiolysis in the exposed ice on Callisto's surface is an insufficient source to produce the amount of O₂ inferred from observations

Correspondence to:

S. R. Carberry Mogan,
carberrymogan@berkeley.edu

Citation:

Carberry Mogan, S. R., Liuzzo, L., Poppe, A. R., Simon, S., Szalay, J. R., Tucker, O. J., & Johnson, R. E. (2023). Callisto's atmosphere: The oxygen enigma. *Journal of Geophysical Research: Planets*, 128, e2023JE007894. <https://doi.org/10.1029/2023JE007894>

Received 8 MAY 2023
Accepted 23 AUG 2023

Author Contributions:

Conceptualization: Shane R. Carberry Mogan, Lucas Liuzzo, Andrew R. Poppe, Sven Simon
Data curation: Jamey R. Szalay
Formal analysis: Shane R. Carberry Mogan, Lucas Liuzzo, Andrew R. Poppe, Sven Simon
Funding acquisition: Lucas Liuzzo, Andrew R. Poppe, Sven Simon
Investigation: Shane R. Carberry Mogan, Lucas Liuzzo, Andrew R. Poppe, Sven Simon
Methodology: Shane R. Carberry Mogan, Lucas Liuzzo, Andrew R. Poppe, Sven Simon, Robert E. Johnson
Project Administration: Lucas Liuzzo, Andrew R. Poppe
Resources: Shane R. Carberry Mogan, Lucas Liuzzo, Sven Simon

© 2023. The Authors.

This is an open access article under the terms of the [Creative Commons Attribution License](https://creativecommons.org/licenses/by/4.0/), which permits use, distribution and reproduction in any medium, provided the original work is properly cited.

Abstract Observations of Callisto's atmosphere have indicated an O₂ component should exist, but the evolution from its initial source to its inferred steady-state abundance is not well understood. Herein we constrain the production of O₂ via radiolysis within Callisto's exposed ice patches and determine the corresponding O₂ column density. To do so, for the first time we simulate the thermal and energetic components of the Jovian magnetospheric plasma irradiating Callisto's atmosphere and estimate energy deposited therein by the impinging charged particles along their trajectories to the surface. We then calculate O₂ source fluxes corresponding to the energy of the impacting plasma fluxes, which is coupled with estimated atmospheric lifetimes to determine the steady-state abundance of O₂. Our results suggest that production of O₂ via radiolysis within the exposed ice on Callisto's surface does not produce a sufficiently dense atmosphere relative to the column densities inferred from observations by about 2–3 orders of magnitude. To resolve this discrepancy between estimated and observed abundances, we provide the first estimates for other potential sources of atmospheric O₂. We also make similar estimates for the production of H₂ in Callisto's atmosphere relative to constraints provided in the literature, and the conclusion is the same: a sufficiently dense atmosphere is not produced. Thus, we have shown that a better understanding of the production and fate of radiolytic products in Callisto's regolith is required in order to place firmer constraints on the generation mechanisms of its atmosphere in preparation for future observations.

Plain Language Summary Molecular oxygen (O₂) has been inferred to exist in Callisto's atmosphere from observations taken across more than two decades by three separate instruments each using distinct measurement techniques. Exposure of Callisto's icy surface by the ions and electrons trapped in Jupiter's magnetic field is expected to produce O₂, which subsequently releases into an atmosphere around Callisto. However, prior to this study, the amount of O₂ produced through such pathways has not been explicitly quantified. Here, for the first time, we determine the amount of O₂ produced by the irradiation of the exposed ice on Callisto's surface by Jupiter's plasma after depositing energy in the atmosphere. Our results show that this source of O₂ does not produce nearly enough compared to what has been inferred from observations. Therefore, additional production mechanisms of O₂ are required at Callisto.

1. Introduction

Following the *Pioneer* discovery of intense plasma trapped within the Jovian magnetosphere (Frank et al., 1976; Smith et al., 1974; Wolfe et al., 1974) a series of experiments were carried out to determine the influence this plasma could have on the surfaces of the icy Galilean satellites, Europa, Ganymede, and Callisto. These experiments measured the ejection of water molecules from low-temperature ices by incident charged particles (Brown et al., 1978; Lanzerotti et al., 1978), a process referred to as sputtering. The results showed that the sputtering of H₂O-ice is dominated by electronic excitations and ionizations produced in the ice (electronic sputtering), rather than by knock-on collisions of the ions with water molecules (nuclear sputtering), the hitherto typically studied sputtering process. Subsequent experiments led to the discovery that the bonds in H₂O-ice molecules can be dissociated by the electronic energy deposited by the impinging charged particles, and the fragmented molecules can recombine to form new species, such as H₂ and O₂, in a phenomenon referred to as radiolysis (Boring et al., 1983; Brown et al., 1982, 1984; Johnson et al., 1983; Reimann et al., 1984). Moreover, the number of radiolytic products released from the icy surface per each incident charged particle (i.e., the yield) was shown to display a strong temperature dependence (Boring et al., 1983; Brown et al., 1982; Reimann et al., 1984).

Software: Shane R. Carberry Mogan, Lucas Liuzzo, Sven Simon
Supervision: Lucas Liuzzo, Andrew R. Poppe, Sven Simon, Orenthal J. Tucker, Robert E. Johnson
Validation: Shane R. Carberry Mogan, Lucas Liuzzo, Sven Simon
Visualization: Shane R. Carberry Mogan, Lucas Liuzzo
Writing – original draft: Shane R. Carberry Mogan, Lucas Liuzzo, Andrew R. Poppe
Writing – review & editing: Shane R. Carberry Mogan, Lucas Liuzzo, Andrew R. Poppe, Sven Simon, Jamey R. Szalay, Orenthal J. Tucker, Robert E. Johnson

The Jovian magnetospheric plasma to which Callisto, the outermost Galilean satellite (orbiting Jupiter at a distance of 26.3 Jupiter radii, $r_J = 71,492$ km) and the focus of this study, is exposed during its orbit can be broken down into two main populations: low-energy ($E \lesssim 1$ keV) thermal plasma and high-energy ($E \gtrsim 1$ keV) energetic particles, both of which are comprised of electrons, protons, and oxygen and sulfur ions (e.g., Kivelson et al., 2004; Mauk et al., 2004). The thermal plasma nearly corotates with the Jovian magnetic field at Callisto's orbital position and impinges onto the moon's orbital trailing hemisphere (TH) at an average relative velocity of ~ 190 km/s (Kivelson et al., 2004). As the thermal plasma overtakes Callisto, the frozen-in magnetospheric field piles-up at the moon's orbital TH and drapes around the moon's ionosphere and induced magnetic field (Liuzzo et al., 2015, 2016). This interaction generates perturbations in the magnetic field and plasma flow, which is deflected around the moon (see also Strobel et al., 2002). The energetic particles bounce rapidly along Jupiter's closed field lines, in addition to drifting azimuthally throughout the magnetosphere. As they approach Callisto, the energetic particles experience the electromagnetic field perturbations generated by this plasma interaction and their resulting precipitation patterns onto the moon are highly non-uniform (e.g., Liuzzo et al., 2019a, 2019b, 2022). There is also variability in the local plasma environment to which Callisto is exposed. Due to the nearly 10° tilt between the Jovian magnetic and rotation axes, the magnetospheric field continuously wobbles with respect to Callisto's orbital plane, and the ambient magnetospheric plasma number density varies by an order of magnitude (see Bagenal & Delamere, 2011; Kivelson et al., 2004). As a result, Callisto's magnetospheric environment is subject to periodic variations (Kivelson et al., 2004), with an M-shell, the radial distance at which a given field line crosses the magnetic equator, that varies from a minimum of $M = 26.3$ out to 70 (Liuzzo et al., 2019a; Paranicas et al., 2018).

The precipitation of the incident magnetospheric plasma onto Callisto's surface leads to a plethora of complicated dynamics. After the plasma impacts the icy surface, neutral atoms and molecules are sputtered and produced via radiolysis, contributing to the formation of Callisto's atmosphere (e.g., Carberry Mogan et al., 2022). These neutral particles can, in turn, be ionized via interactions with solar photons and the incident plasma. The nascent charged particles contribute to the formation of Callisto's ionosphere while also being picked up and accelerated by the local electromagnetic fields. These picked-up ions contribute to mass loading and diversion of the magnetospheric plasma flow, which can act to partially suppress the ion precipitation and thus atmosphere formation. Further, such processes can lead to a self-limiting atmosphere. As the abundance of the atmosphere increases, the impinging plasma has to penetrate the atmosphere, where it can deposit some or all of its energy therein (as well as dissociate and/or ionize atmospheric molecules) along its trajectory to the surface. If the plasma successfully penetrates the atmosphere but deposits some of its energy therein, the sputtering and radiolysis yields can be diminished as a result of the incident charged particles' reduced energy. This could result in a decrease in atmospheric production via sputtering, which would in turn lead to a decrease in atmospheric density such that the impinging plasma will deposit less or no energy in the atmosphere prior to impacting the surface, which in turn increases the atmospheric production rates, and so on. Theoretically, this process should continue until a steady-state is attained. Other additional sources of the atmosphere, such as sublimation of water-ice, can contribute to the above complexities. However, recent modeling efforts (Carberry Mogan et al., 2022) suggest that sublimated H_2O is a minor component of Callisto's atmosphere relative to the radiolytic products O_2 and H_2 .

Indeed, such interrelated dynamics between Callisto's surface and atmosphere and the Jovian magnetosphere are likely the primary source of the inferred O_2 atmosphere at Callisto (e.g., Cunningham et al., 2015; de Kleer et al., 2023; Kliore et al., 2002). That is, O_2 is primarily produced via radiolysis and subsequently released from the surface (e.g., Teolis et al., 2017). Upon release from the surface, since O_2 is too heavy and slow to escape the atmosphere and reactions therein are infrequent, it will eventually return to the surface. However, O_2 is too volatile to freeze out at Callisto's surface temperatures, so it will permeate the porous regolith (e.g., Johnson et al., 2019). Since O_2 is a relatively inert molecule, reactions in the regolith are infrequent, so that it will eventually thermally desorb back into the atmosphere. This enrichment process is thus primarily limited by the infrequent gas-phase ionizing and dissociative processes, such that even a relatively small source rate can result in a relatively thick, collisional atmosphere (e.g., Carberry Mogan et al., 2020, 2021, 2022).

Constraining radiolytic production of O_2 at Callisto is extremely difficult, not only because of the uncertainties described above pertaining to the local plasma environment but also due to the uncertainty of its surface composition, in particular the abundance and spatial distribution of H_2O -ice. Estimates for surficial coverage of ice on its leading hemisphere (LH) and TH range from only 5%–30% (Clark & McCord, 1980; Mandeville et al., 1980; McCord et al., 1998; Pilcher et al., 1972; Roush et al., 1990; Spencer, 1987a) with an additional 0%–10% bound

water (Clark & McCord, 1980), while the remainder is a relatively dark silicate and/or carbonaceous material (McCord et al., 1998). However, these ranges only refer to *exposed* ice patches on its surface, and others have suggested that the ice is intimately mixed with the non-ice surface material with weight fractions ranging from 20 to 90 wt% (Calvin & Clark, 1991; Clark, 1980; McCord et al., 1998; Roush et al., 1990) with an additional 0–10 wt% bound water (Clark, 1980). Radiolysis can be readily induced in the exposed H₂O-ice patches producing O₂ (and H₂). In addition, O₂ (and H₂), as well as other species, such as CO₂ (Carlson, 1999; Hendrix & Johnson, 2008), can be produced via radiolysis in the non-ice or ice-poor material on Callisto's surface, thereby supplying an additional, difficult-to-constrain source for the atmosphere.

As described in detail in Section 2, although measurements by *Galileo*, the Hubble Space Telescope (HST), and Earth-based telescopes inferred an O₂ atmosphere should exist at Callisto, the evolution from its initial source to its inferred steady-state abundance as well as its temporal and spatial variability are still not well understood. Here we attempt to address the aforementioned uncertainties regarding Callisto's O₂ atmosphere by constraining its radiolytic production from the exposed ice patches as well as its corresponding steady-state abundance. We emphasize that this study implements a first-principles approach to try to answer the question: Can our present knowledge of Callisto's plasma environment and radiolytic production mechanisms account for the inferred density of O₂ in Callisto's atmosphere? To do so, we simulate the fluxes of thermal plasma and energetic particles irradiating Callisto's atmosphere and surface to determine the initial radiolytic O₂ source flux and corresponding column density of O₂ (Sections 3 and 4). Finally, in Section 5, we discuss the implications of our results, in particular how they compare to values inferred from observations; as well as provide estimates for other potential sources of O₂ in Callisto's atmosphere, the first such constraints in preparation for future observations, such as those that will be made by the JUPITER ICy moons Explorer (JUICE), Europa Clipper, and HST.

2. Background

Radio occultations made by *Galileo* indicated the presence of a substantial ionosphere with peak electron densities of $\sim 10^4 \text{ cm}^{-3}$ located close to Callisto's surface near the terminator (Kliore et al., 2002). Analogous to the O₂ atmosphere on Europa inferred from oxygen emissions (Hall et al., 1995), Callisto's ionosphere was suggested to be produced from a relatively dense ($\sim (1-3) \times 10^{10} \text{ cm}^{-3}$) and thus collisional O₂ atmosphere. This substantial, near-surface ionosphere was only seen at western elongation: when the TH of Callisto is simultaneously illuminated by the Sun and bombarded by the co-rotating Jovian magnetospheric plasma. Ionospheric electrons were also detected by *Galileo*'s plasma-wave instrument far from Callisto's surface ($\sim 1.2-2.0 r_C$, where $r_C = 2,410 \text{ km}$ is the radius of Callisto) when Callisto was at eastern elongation (Gurnett et al., 1997, 2000); that is, when Callisto's LH, which is opposite its ram-side hemisphere, is illuminated. However, Carberry Mogan et al. (2022) recently suggested that these electrons may have been produced via the extended H₂ component in Callisto's atmosphere.

Atomic oxygen emissions were detected using the HST-Cosmic Origins Spectrograph (COS) (Cunningham et al., 2015), which were suggested to be induced by photoelectron impacts in a near-surface, O₂-dominated atmosphere when Callisto was at eastern elongation. The inferred disk-averaged O₂ column density, $\sim 4 \times 10^{15} \text{ cm}^{-2}$, is an order of magnitude less than that inferred by Kliore et al. (2002) at western elongation, $\sim 4 \times 10^{16} \text{ cm}^{-2}$. Nevertheless, this reduced estimate made by Cunningham et al. (2015) still implies that Callisto has the densest atmosphere among the icy Galilean satellites, and its atmosphere is only exceeded in mass among other satellites in the Solar System by Io, Titan, and Triton.

Recently, de Kleer et al. (2023) observed auroral emissions emanating from Callisto's atmosphere while the satellite was in eclipse, which was interpreted as originating from an O₂ component. Unlike the observation of Cunningham et al. (2015), photoelectrons could not be the source of the emissions since Callisto was shielded from photons by Jupiter. Therefore, de Kleer et al. (2023) suggested magnetospheric electrons were responsible for producing the emissions. Despite these suggested difference in sources, photo- versus magnetospheric electron impacts, Cunningham et al. (2015) and de Kleer et al. (2023) both arrived at roughly the same disk-averaged column density of O₂ required to produce the detected emissions: $\sim 4 \times 10^{15} \text{ cm}^{-2}$. Although Cunningham et al. (2015) ultimately ruled out magnetospheric electrons as a source of the emissions, they still made a theoretical estimate for the emissions produced via magnetospheric electron impacts, which proved to be insufficient anyway. Interestingly, de Kleer et al. (2023) applied a similar electron flux as that assumed by Cunningham et al. (2015) to estimate the emission production in their theoretical estimate.

Modeling efforts over the same time-span of the above observations have complemented these constraints. Liang et al. (2005) applied 1D chemistry models in Callisto's atmosphere assumed to be composed of O₂, H₂O, and CO₂, as well as the resulting neutrals and ions formed via reactions to reproduce the electron densities detected by Kliore et al. (2002) while satisfying the upper limits of atmospheric densities (Strobel et al., 2002). Hartkorn et al. (2017) implemented an analytic O₂ + CO₂ + H₂O atmosphere in a 3D ionosphere model where photo-ionization and collisions between photoelectrons and neutrals were the sources of the ionospheric electrons and ultraviolet (UV) emissions to explain the ionospheric observations made by Kliore et al. (2002) and the UV emissions observed by Cunningham et al. (2015). Vorburger et al. (2015) applied a 1D Monte Carlo model to simulate several sources and sinks of ice- and non-ice-related species in an assumed surface-bound exosphere. Vorburger et al. (2019) improved on their earlier work by expanding the model to 3D and differentiating between cold and hot magnetospheric plasma sputtering of the surface. This study also considered the influence of ionospheric shielding by assuming that when an ionosphere was present, only the energetic particles could impact the surface and did so isotropically, otherwise both the thermal plasma and energetic particles impacted the surface with the former preferentially impacting the TH. Carberry Mogan et al. (2020) applied 1D molecular kinetics models to simulate intermolecular collisions and thermal escape in atmospheres on Callisto composed of radiolytically produced CO₂, O₂, and H₂, all of which were assumed to permeate the porous regolith and thermally desorb therefrom. Carberry Mogan et al. (2021) followed up on this work by expanding the model to 2D to include the diurnal variation of Callisto's surface temperatures and the corresponding local and global transport, as well as sublimated water vapor. They compared the production of H via photodissociation of sublimated water vapor to that of radiolytically produced H₂ and suggested the latter is the primary source of the detected H corona (Roth et al., 2017). Carberry Mogan et al. (2022) affirmed this notion by simulating the production of H via dissociative processes in an H₂O + H₂ + O₂ + H atmosphere and showed that indeed radiolytically produced H₂ is the primary source of the detected H, and is also capable of producing the enhanced electrons detected by *Galileo* far from Callisto (Gurnett et al., 1997, 2000). Carberry Mogan et al. (2022) also provided constraints on the required source rates for radiolytically produced H₂ and initial estimates for an H₂ torus co-orbiting with Callisto, as well as maximum sublimation rates and corresponding densities of H₂O, both of which suggest that all previous modeling efforts that considered H₂O in Callisto's atmosphere overestimated its abundance by 1–2 orders of magnitude (Carberry Mogan et al., 2021; Hartkorn et al., 2017; Liang et al., 2005; Vorburger et al., 2015).

Except for Vorburger et al. (2019), all of the above mentioned modeling efforts were guided by observations to simulate their atmosphere: they either used the densities inferred from observations as inputs or as results to reproduce. Vorburger et al. (2019), on the other hand, implemented ion sputtering at Callisto to simulate ab initio production of O₂ as well as several other species. However, they did not consider that the interaction between Callisto's ionosphere and magnetospheric environment perturbs the local electromagnetic fields and alters the plasma precipitation patterns onto Callisto's surface, which plays an especially important role for electrons and low-energy ions (e.g., Liuzzo et al., 2022). Moreover, they assumed that if the sputtered particles returned to the surface they would “stick” with unity efficiency and are thus no longer considered in the simulation. Since O₂ does not escape Callisto's atmosphere, and reactions therein are infrequent, it will primarily return to the surface. This process will be the dominant sink for O₂. As a result, the O₂ densities estimated by Vorburger et al. (2019) were ~7–8 orders of magnitude less than those inferred from observations: ~10² cm⁻³ (see Figures 4 and 5 therein) compared to ~10⁹–10¹⁰ cm⁻³.

3. Method

Below we first describe the methods used to simulate Callisto's electromagnetic environment (Section 3.1). Next, we derive a temperature distribution for Callisto's ice patches (Section 3.2). This distribution is then used to analytically calculate O₂ atmospheres, which are used to estimate energy deposited therein by the impinging Jovian magnetospheric plasma along its trajectory to the surface (Section 3.3), as well as calculate the O₂ radiolytic production yields (Section 3.4), which are used to determine the O₂ source fluxes corresponding to the energy of the plasma components impacting Callisto's icy surface (Section 4).

3.1. Modeling Callisto's Electromagnetic Environment

To accurately represent the dynamics of particles as they travel through Callisto's perturbed electromagnetic environment before depositing energy into the moon's atmosphere and surface, we apply two separate models. The

first is the Adaptive Ion-Kinetic, Electron-Fluid (AIKEF) model (Liuzzo et al., 2015; Müller et al., 2011), which is a hybrid plasma model that treats thermal ions as individual particles and thermal electrons as a massless, charge-neutralizing fluid. This representation of the charged particles near Callisto allows for the resolution of ion-kinetic effects, including flow shear between multiple plasma species and an accurate treatment of large ion gyroradii, both of which are important features of Callisto's interaction with the Jovian magnetospheric plasma (Liuzzo et al., 2016, 2017, 2018). The second is the Galilean Energetics Tracing Model (GENTOO), which is a test particle model that solves the relativistic Lorentz force equation for energetic ions and electrons (Liuzzo et al., 2019a, 2019b). GENTOO calculates the trajectories of these particles as they travel through the perturbed electromagnetic fields near Callisto (obtained from AIKEF) and calculates the flux deposited by the energetic particles as they precipitate onto a prescribed lower boundary.

This study uses the results from Liuzzo et al. (2022). These authors combined output from AIKEF with GENTOO to constrain the energetic electron, proton, and oxygen and sulfur ion fluxes onto the top of Callisto's atmosphere for three positions of the moon with respect to the center of the Jovian magnetospheric current sheet. These authors illustrated that, because of the variability of the magnetospheric environment over a full synodic period, the ion and electron fluxes deposited onto the moon's atmosphere when located near the current sheet center exceed those when the moon is far from the center by at least an order of magnitude. Thus, since most of the irradiation takes place near the center of the sheet, this case is “representative” of the flux deposited over a full synodic rotation, despite Callisto spending only a short amount of time in this region. For this reason, we apply the fluxes from Liuzzo et al. (2022) with Callisto located at the center of the current sheet for this study. For a comprehensive discussion of the properties associated with Callisto's perturbed electromagnetic environment, as well as its effect on the dynamics of charged particles and their resulting fluxes onto the top of the moon's atmosphere, the reader is referred to that study.

In their study, Liuzzo et al. (2022) constrained the particle fluxes onto the top of Callisto's atmosphere, defined to be located at an altitude of $1.1r_c$. Below these altitudes, interactions and collisions with Callisto's atmosphere may cause energy loss of the incident ions and electrons, physical processes that are not included in the GENTOO approach. These authors investigated energetic ions and electrons at energies $4.5 \text{ keV} \leq E \leq 24 \text{ MeV}$, but did not calculate the deposited fluxes associated with the thermal ($E \lesssim 1 \text{ keV}$) plasma. Therefore, we apply the method of Liuzzo et al. (2022) to calculate ion and electron fluxes onto the top of Callisto's atmosphere for energies $34 \text{ eV} \lesssim E < 4.5 \text{ keV}$. This lower range is below the peak plasma energy near Callisto (see Figure 1) and is also close to the minimum particle energy required for radiolysis on icy surfaces to occur ($\sim 10 \text{ eV}$; e.g., Orlando & Sieger, 2003). Hence, extending the results of Liuzzo et al. (2022) to lower energies provides the flux of particles at energies $34 \text{ eV} \lesssim E \leq 24 \text{ MeV}$, which adequately covers the range of energies near Callisto's orbital position at which particles impinge onto the moon.

Figure 1 displays the particle energy spectra in the unperturbed plasma outside of Callisto's interaction region for all four species studied here. The curves used by Liuzzo et al. (2022) to calculate the energetic particle fluxes are included in blue for ions (obtained from Mauk et al., 2004), and in blue (Garrett et al., 2003) and orange (Jun et al., 2019) for electrons. At lower energies, yellow curves represent a Maxwellian fit to the thermal plasma populations near Callisto. In addition to these curves, data from the Juno spacecraft are included as green and red dots in Figure 1. For further detail, see Appendix A.

3.2. Surface Temperature

We assume that Callisto's surface is segregated into patches of relatively cold, bright ice and relatively warm, dark non-ice or ice-poor material. We apply a conservative estimate from the literature for the surficial coverage of ice of 10% (Spencer, 1987a), and due to the lack of high resolution imaging over the entire surface, we assume the ice patches are uniformly distributed throughout the surface. Assuming heat conduction between the bright ice with higher thermal inertia and the dark non-ice or ice-poor material with lower thermal inertia is negligible, the temperatures of these two surface components can remain independent from one another. Grundy et al. (1999) derived disk-averaged H_2O -ice temperatures at Callisto using the temperature dependence of the near-infrared water-ice reflectance spectrum. These temperatures are representative of the sparse, bright ice patches, which are distinct from the predominant, dark non-ice or ice-poor material observed to be much warmer (e.g., Moore et al., 2004; Spencer, 1987c).

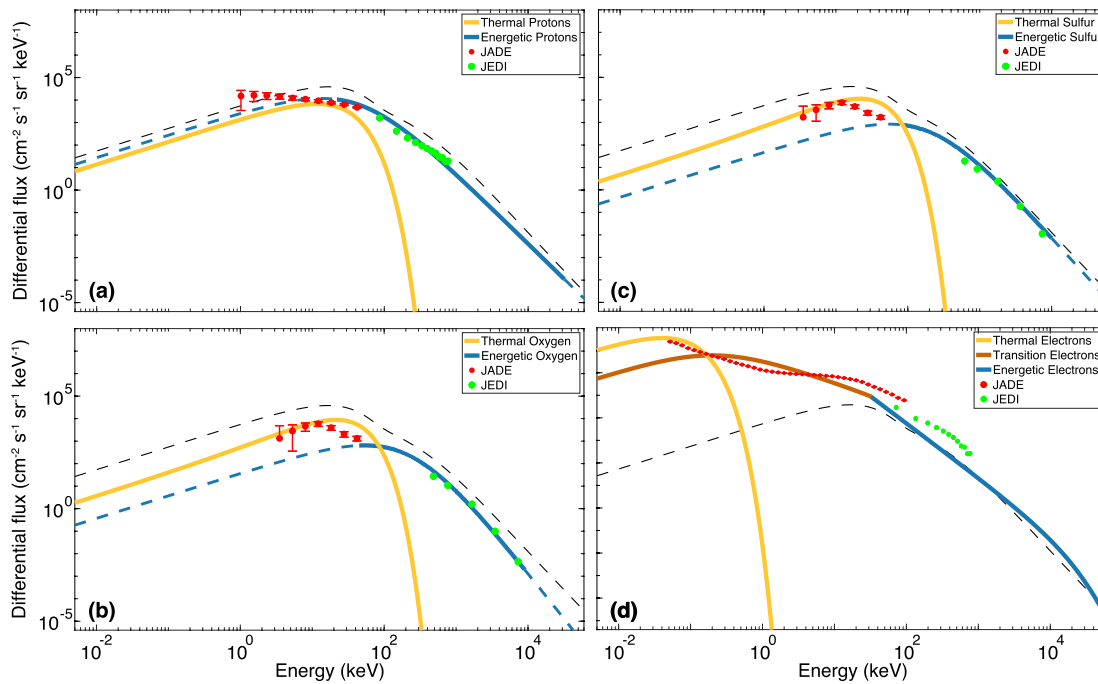


Figure 1. Differential number flux spectra for (a) protons, (b) oxygen ions, (c) sulfur ions, and (d) electrons near Callisto's orbit. Curves illustrate fits for the (yellow) thermal and (blue) energetic plasma. Orange curves for electrons represent the transition from thermal to energetic regime. Red and green points denote observations of each population from Juno while located near Callisto's orbital position. The black dashed line in each panel illustrates the sum of the differential ion fluxes over all ion species. See text and Appendix A for further detail.

As described in Appendix B, we generate a temperature distribution for the ice patches, T_{ice} , as a function of solar zenith angle (χ) according to the disk-averaged ice temperatures derived by Grundy et al. (1999), assuming a minimum surface temperature of 80 K (e.g., Carberry Mogan et al., 2022 and references therein). The resulting temperature distribution, which is an improvement to that derived by Carberry Mogan et al. (2022), is illustrated in Figure 2. Since we assume that the exposed ice patches only cover about 10% of the surface and they are uniformly distributed throughout the surface, Figure 2 represents a map of the local ice temperature for a given latitude and longitude. In this temperature distribution, $T_{ice} \sim 144$ K at the subsolar point ($\chi = 0^\circ$), which is located at 0° Latitude, 270° W. Longitude in Figure 2; that is, Callisto is situated at western elongation (18:00 Jovian local time). We did not implement, for example, a thermal inertia model to determine how the surface temperature varies during Callisto's orbit, as has been done at the other Galilean satellites (Addison et al., 2022;

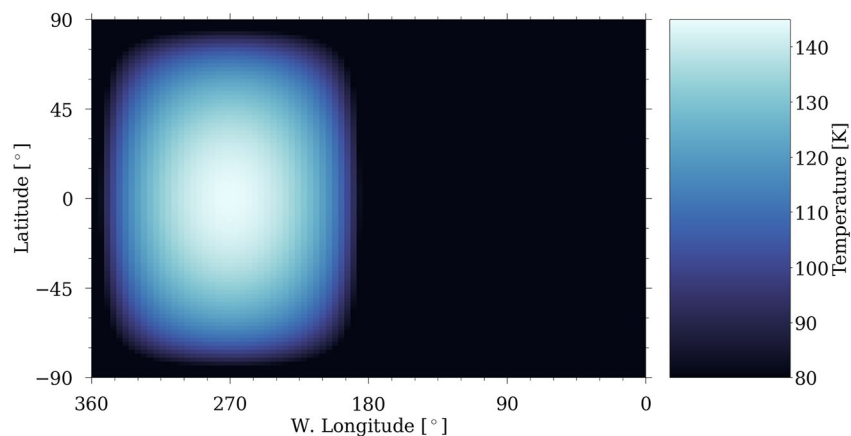


Figure 2. Surface temperature distribution for the segregated ice patches, T_{ice} , where a minimum temperature of 80 K is implemented and the subsolar point is located at 0° Latitude, 270° W. Longitude.

Leblanc et al., 2017; Walker et al., 2012). However, since Callisto's orbital period is much longer than that of those bodies, we expect such changes to be comparatively less important. Moreover, any such changes do not change the principal conclusion of this study.

3.3. Modeling Energy Deposition in Callisto's Atmosphere

When simulating energy deposition in Callisto's atmosphere, we consider two sample O₂ components assuming uniform surface density, $n_0 = 10^9 \text{ cm}^{-3}$ and $n_0 = 10^{10} \text{ cm}^{-3}$. As demonstrated by Carberry Mogan et al. (2022), the former n_0 can produce the disk-averaged column densities inferred by Cunningham et al. (2015) and de Kleer et al. (2023), while the latter n_0 is the densest estimate inferred from observations (Kliore et al., 2002).

We generate a 3D atmosphere analytically based on these prescribed n_0 , while implementing the same latitudinal and longitudinal coordinates as in GENTOO: a 2° resolution in latitude, ϕ , and a 4° resolution in longitude, θ . We assume an isothermal temperature profile above each of these surface cells: $T(r, \phi, \theta) = T(r_C, \phi, \theta)$, where $r_C = 2,410 \text{ km}$ is the radius of Callisto, r is the radial altitude up to $1.1 r_C$ (241 km above r_C), and $T(r_C, \phi, \theta)$ is the local surface temperature. Although we assume that O₂ is produced from the ice patches with the temperature distribution illustrated in Figure 2 with a minimum surface temperature of 80 K, on return to the surface we assume they re-desorb from either the ice or non-ice patches, where the latter is assumed to have the temperature distribution illustrated in Figure 1a in Carberry Mogan et al. (2022). As a result, on the day-side we calculate an average surface temperature weighted by the surficial coverage, 10% ice and 90% non-ice. From 1.0 to $1.1 r_C$, we set the radial extent of each cell, Δr , equal to the local mean free path, ℓ_{MFP} , where an approximate O₂-O₂ collision cross-section of $5 \times 10^{-15} \text{ cm}^2$ is implemented, or 1 km if $\ell_{\text{MFP}} > 1 \text{ km}$. We then calculate the local atmospheric number density as a function of r via the following equation:

$$n(r, \phi, \theta) = n_0 \exp\left(-\lambda\left(1 - \frac{r_C}{r}\right)\right). \quad (1)$$

Here $\lambda = \frac{GM_C m_{\text{O}_2}}{kr_C T(r_C, \phi, \theta)}$ is the Jeans parameter, which is the ratio of an O₂ molecule's gravitational binding energy to Callisto ($GM_C m_{\text{O}_2}/r_C$) to its thermal energy ($k_B T(r_C, \phi, \theta)$), where G is the gravitational constant, $M_C = 1.08 \times 10^{23} \text{ kg}$ is the mass of Callisto, and $m_{\text{O}_2} = 32 \text{ amu}$ is the mass of an O₂ molecule.

After generating the model atmospheres, we estimate the energy deposited therein by the energy-dependent incident number fluxes of thermal plasma and energetic particles at $\sim 1.1 r_C$ obtained from GENTOO (Section 3.1) along their trajectories to Callisto's surface. To do so, we calculate the local stopping power with depth into the atmosphere, $\frac{dE}{dr}(r, \phi, \theta)$, via the following equation:

$$\frac{dE}{dr}(r, \phi, \theta) = n(r, \phi, \theta) S(E). \quad (2)$$

Here $S(E) = S_n(E) + S_e(E)$ for the ions and $S(E) = S_e(E) + S_r(E)$ for the electrons; and S_n , S_e , and S_r are the nuclear, electronic, and radiative stopping cross-sections, respectively (see Figure C2a in Appendix C). Due to the lack of data for S_e for electrons penetrating gaseous O₂ below 1 keV, we extrapolate the slope of S_e between 1 and 1.5 keV and apply that for $E < 1 \text{ keV}$. Equation 2 is calculated for all of the energies considered across every point in latitude and longitude, from an altitude of $1.1 r_C$ down to $1 r_C$. The energy at the bottom of one cell, $E(r_1) = E(r_2) - dE$, is the initial energy at the top of the cell below that, and so on until reaching the surface, where the final energies are calculated.

Note we only consider the O₂ component of Callisto's atmosphere, and thus neglect energy deposition in Callisto's extended H₂ atmosphere (e.g., Carberry Mogan et al., 2022), which is produced via radiolysis in water-ice in a stoichiometric ratio of 2:1 with O₂. We also neglect energy deposition in any H₂O component produced via sublimation and sputtering from the sparse and cold ice patches, because the H₂O particles condense to the ice and/or react in the regolith, so that the corresponding densities will be minor relative to that of the O₂ component (e.g., Carberry Mogan et al., 2022). Finally, we also neglect any energy deposition in the CO₂ component in Callisto's atmosphere (Carlson, 1999), which was suggested to be up to 25× less dense than O₂ at Callisto's surface, and thus energy deposition within any CO₂ component is expected to be negligible in comparison. Nevertheless, these results represent an upper limit, since any additional atmospheric components would further reduce the energy of impinging charged particles along their trajectories to the surface.

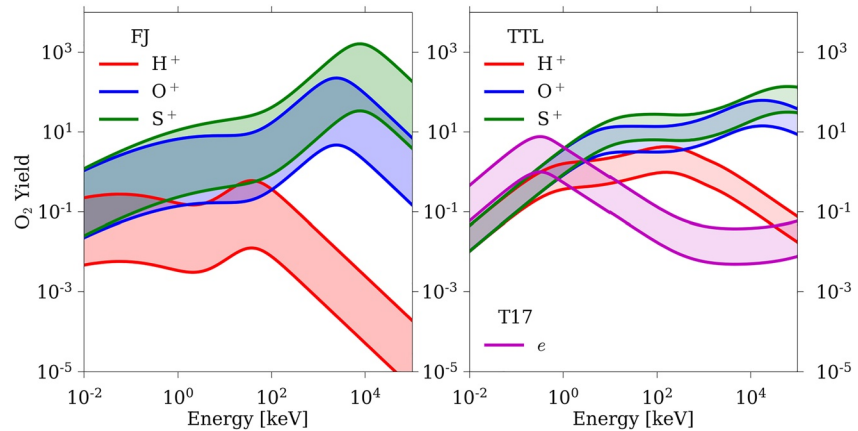


Figure 3. O_2 yields, Y_{O_2} , estimated via the FJ (left panel) and TTL (right panel) formulae for H^+ (red lines), O^+ (blue lines), and S^+ (green lines) over an energy range of $10 \text{ eV} \leq E \leq 100 \text{ MeV}$. Y_{O_2} for penetrating electrons (magenta lines) are estimated using the original formula and constants from Teolis et al. (2017), “T17” (right panel), over the same energy range. The shaded regions represent the range in yields between the lower and upper bounds (solid lines) estimated at the minimum and maximum surface temperatures of Callisto’s surface ice, 80 and 144 K (Figure 2), respectively. Note that the projected ranges for electrons with $E < 10 \text{ keV}$ are calculated differently than those with $10 \text{ keV} \leq E \leq 12 \text{ MeV}$ (see Appendix C), causing a slight discontinuity in the corresponding Y_{O_2} at $E = 10 \text{ keV}$.

3.4. Yield

Ignoring any possible production of O_2 via radiolysis in the non-ice or ice-poor material and/or in the underlying ice, here we estimate the O_2 yield solely from Callisto’s exposed ice patches. Writing the yield of O_2 is somewhat misleading as the radiolytic production process for O_2 is fundamentally different from that of the sputtered H_2O , for which the term is more suitably applied. That is, whereas sputtering of H_2O is a surface process, O_2 is radiolytically produced at depth within the ice so that the yield is primarily controlled by diffusion through the irradiated ice and subsequent release therefrom (e.g., Teolis et al., 2017). However, if O_2 accumulates near the surface, for example, in voids in the radiation-damaged ice (e.g., Johnson & Jesser, 1997; Spencer & Calvin, 2002), then such a reservoir of O_2 can be prone to sputtering, albeit the yield for higher-energy sputtered O_2 is orders of magnitude lower than that for lower-energy thermal release of O_2 (e.g., Johnson et al., 1983; Figure 2 therein). Moreover, the O_2 can also be destroyed in these reservoirs by continued irradiation instead of being ejected. Nevertheless, we use the term yield throughout this study when describing the radiolytic production of O_2 .

Using the results from Appendix C, we calculate O_2 radiolytic production yields, Y_{O_2} , induced by impinging ions via two alternative techniques: implementing (a) a combination of formulae from Famá et al. (2008) and Johnson et al. (2009), hereafter referred to as the “FJ” formula; and (b) the formula from Teolis et al. (2017) with updated values from Tribbett and Loeffler (2021), hereafter referred to as the “TTL” formula. Since the FJ formula does not estimate Y_{O_2} for impinging electrons, we use the original values from the formula of Teolis et al. (2017), hereafter referred to as the “T17” formula and, depending on the energy, apply either the continuous-slowing-down approximation (CSDA) range (for $E \geq 10 \text{ keV}$) or an analytic estimate from the literature for their projected ranges, R_p (for $E < 10 \text{ keV}$). See Appendix D for more detailed descriptions of these calculations.

In Figure 3, we compare the O_2 yields produced with the FJ formula to those produced with the TTL formula for the impinging ions corresponding to the minimum and maximum ice temperatures, 80 K (lower bounds in Figure 3) and $\sim 144 \text{ K}$ (upper bounds in Figure 3), respectively. There are two major differences in the energy dependencies of Y_{O_2} between the former and latter formula. First, at ion energies $\lesssim 100 \text{ keV}$, $(Y_{O_2})_{\text{ion,FJ}}$ is proportional to S_n , while $(Y_{O_2})_{\text{ion,TTL}}$ is proportional to E so long as $R_p < x_0$. Second, at ion energies $> 100 \text{ keV}$, $(Y_{O_2})_{\text{ion,FJ}}$ is proportional to S_e^2 , while $(Y_{O_2})_{\text{ion,TTL}}$ is proportional to the total stopping power (Teolis et al., 2017). As can be seen, the difference in Y_{O_2} between these formula are the most pronounced for protons (red lines in Figure 3). This is because the stopping cross-sections for impinging protons (both S_n and S_e) and thus $(Y_{O_2})_{H^+,FJ}$ are relatively small below $\sim 100 \text{ keV}$ (Figure C1a in Appendix C); and after reaching a maximum around $\sim 100 \text{ keV}$, S_e and $(Y_{O_2})_{H^+,FJ}$ begin to exponentially decrease with increasing E (S_n for protons reaches a maximum around $\sim 100 \text{ eV}$ and exponentially decreases thereafter). On the other hand, $(Y_{O_2})_{H^+,TTL}$ steadily increases until around $\sim 100 \text{ keV}$,

before more gradually decreasing with increasing E due to the increasing R_p . The differences between Y_{O_2} for impinging oxygen and sulfur ions are not nearly as significant, as the lower and upper bounds for $(Y_{O_2})_{O^+,S^+;TTL}$ essentially fall within those for $(Y_{O_2})_{O^+,S^+;FJ}$.

As can also be seen in Figure 3, and consistent with Teolis et al. (2017), there is a falloff in Y_{O_2} above ~ 400 eV for electrons as they become so highly penetrating that the energy delivered to the ~ 30 Å surface layer declines with increasing electron energy, making electrons less efficient at producing O_2 (per eV deposited energy) than less penetrating ions. Note this falloff in Y_{O_2} above ~ 400 eV is in contrast to the experimental results reported by Galli et al. (2018), which showed O_2 yields remaining roughly constant after this peak out to ~ 10 keV. However, since the energies considered by Galli et al. (2018) only extend to ~ 10 keV and we are interested in energies as high as ~ 24 MeV, we thus implement the T17 formula as it provides a distribution that can be applied across our energy range of interest. The yield distribution is seen to flatten out above ~ 1 MeV (between $10^{-1} - 10^{-3}$ depending on the surface temperature), before slightly increasing with increasing energy around ~ 10 MeV; this latter result is due to the increase in energy being greater than the decrease in the ratio between R_p and x_0 , resulting in a positive gradient in yield at such large energies.

3.5. Caveats and Inconsistencies

When estimating energy deposition in Callisto's O_2 atmosphere (Section 3.3), we assumed that the path of the ions and electrons is a straight line such that they travel radially downward from the lower boundary of the GENTOO model (at an altitude of 240 km) to Callisto's surface. While the angle at which these particles impinge onto Callisto may not be radial, we note that ions have gyroradii that exceed the spatial resolution used for the GENTOO and AIKEF models (2° in latitude and 4° in longitude for GENTOO, and ~ 100 km for AIKEF). Hence, the actual path these ions travel within the atmosphere is not much different from a straight line. Notably, electrons at energies $E \lesssim 1$ keV possess gyroradii that are lower than this resolution. However, as will be discussed in Section 4, electrons can deposit all of their incident energy into Callisto's O_2 atmosphere before reaching the surface depending on n_0 : at $n_0 = 10^{10} \text{ cm}^{-3}$ ($n_0 = 10^9 \text{ cm}^{-3}$) electrons with $E \lesssim 0.25$ keV ($E \lesssim 0.1$ keV) will deposit all of their incident energy. Thus, our results represent an *upper limit* for the O_2 generated from incident electrons at energies $E \lesssim 1$ keV.

We also note that there are a few inconsistencies between the atmosphere used within the AIKEF model and that generated here from radiolysis on the surface as well as that implemented in the energy deposition model.

First, the behavior of thermal electrons are treated in two separate ways: within AIKEF as a massless, charge-neutralizing fluid that does not interact with the atmosphere in any way, and by GENTOO and the energy deposition model as particles that lose energy within the atmosphere and deposit energy onto the surface. However, when Callisto is embedded within the Jovian magnetospheric plasma sheet, its plasma interaction is "saturated." That is, the moon's interaction with the plasma causes the ambient convective electric field to be reduced to ~ 0 mV/m near the moon (see, e.g., Liuzzo et al., 2015; Saur et al., 1999, 2013) and the electromagnetic field perturbations resulting from its interaction are maximized. Hence, treating electrons as particles within a plasma interaction simulation would not affect the global electromagnetic perturbations in any meaningful way.

An additional inconsistency between these approaches is that AIKEF applies a prescribed atmospheric profile that is not identical to the atmosphere produced by the charged particle precipitation. In principle, this inconsistency could be addressed by applying the initial results from AIKEF, calculating the charged particle precipitation to generate an O_2 atmosphere via radiolysis, re-running AIKEF with this updated atmosphere model, and repeating this iterative process until convergence is reached. However, because Callisto's interaction is already saturated, this exercise would generate only locally minor, quantitative changes to the electromagnetic fields. The precipitation patterns of the ions and electrons (and the resulting O_2 column produced) would therefore not be strongly affected (see also discussion below). Nevertheless, a self-consistent approach is indeed warranted, and is the subject of future work.

For consistency, we ran an additional AIKEF simulation that is identical to the one presented by Liuzzo et al. (2022) (and used for this study), but with the maximum surface number density of O_2 reduced to $n_{0,O_2} = 10^9 \text{ cm}^{-3}$ within the model. Since Callisto's plasma interaction is saturated near the center of the Jovian plasma sheet, differences in the resulting electromagnetic fields are negligible, and the incident particle fluxes onto the top of Callisto's atmosphere are nearly indistinguishable from the cases presented in Section 4, see Appendix F. We found that

Table 1

Total Radiolytic Production Rates of O₂ Induced by Energetic H⁺, O⁺, S⁺, and e in an O₂ Atmosphere With an Assumed Surface Density of n_{0,O₂} = 10¹⁰ cm⁻³

Plasma	Production rate [(×10 ²³) s ⁻¹]		Percentage of total [%]	
	FJ	TTL	FJ	TTL
H ⁺	0.11	1.6	0.41	7.0
O ⁺	5.0	4.3	18	20
S ⁺	16	8.9	57	41
e	7.0 ^a		24	32
Total	28	22	100	

^aThe O₂ production rate induced by energetic electrons is derived via the original formula from Teolis et al. (2017).

only the low-energy ($E \lesssim 4.5$ keV) electron flux patterns are affected by the ionosphere corresponding to this smaller n_{0,O_2} , but still remained similar (within ~90% of those for the case with larger n_{0,O_2}). Further, as discussed in Section 4, even for the case with a larger density of O₂ at the surface, only particles with $E \lesssim 4.5$ keV deposit appreciable energy into the atmosphere. Thus, any changes in the amount of O₂ produced between these two cases, $n_{0,O_2} = 10^9$ cm⁻³ compared to $n_{0,O_2} = 10^{10}$ cm⁻³, stems from the (slight) differences between the electron fluxes onto the top of the atmosphere, for energies $E \lesssim 4.5$ keV (compare Tables 1 and F1 and Figures 6 and F3). These results from using a surface density of $n_{0,O_2} = 10^9$ cm⁻³ within AIKEF to calculate the electromagnetic field perturbations and resulting charged particle fluxes are presented in Appendix F.

Finally, the analytic model atmospheres used to determine energy deposition according to the two n_{0,O_2} considered here (Section 3.3) are slightly different than those implemented in the AIKEF model, most notably on the night-side. However, for the reasons addressed above, these differences do not affect the principal conclusion of this study.

4. Results

Using the results from GENTOO for magnetospheric particle fluxes at an altitude of 1.1 r_C (Section 3.1), we then need to determine how energy is deposited in Callisto's atmosphere down to the surface, 1.0 r_C . Figure 4 illustrates several instances of energy deposition in Callisto's O₂ atmosphere determined using the model described in Section 3.3 with $n_{0,O_2} = 10^{10}$ cm⁻³ by comparing the energy of the fluxes at the surface, 1.0 r_C , to that at the top of the model atmosphere at 1.1 r_C . The energy above which protons, oxygen ions, sulfur ions, and electrons deposit negligible amounts of energy into Callisto's atmosphere is 259 eV, 4.5 keV, 12 keV, and 1.737 keV, respectively. That is, below these energies, particles lose an appreciable amount of energy as they pass through Callisto's atmosphere, from an altitude of 1.1 r_C down to the surface. Energy deposition is especially significant for low-energy O⁺ ions ($E(1.1r_C) < 100$ eV) and S⁺ ions ($E(1.1r_C) < 259$ eV) as well as electrons ($E(1.1r_C) < 259$ eV), where

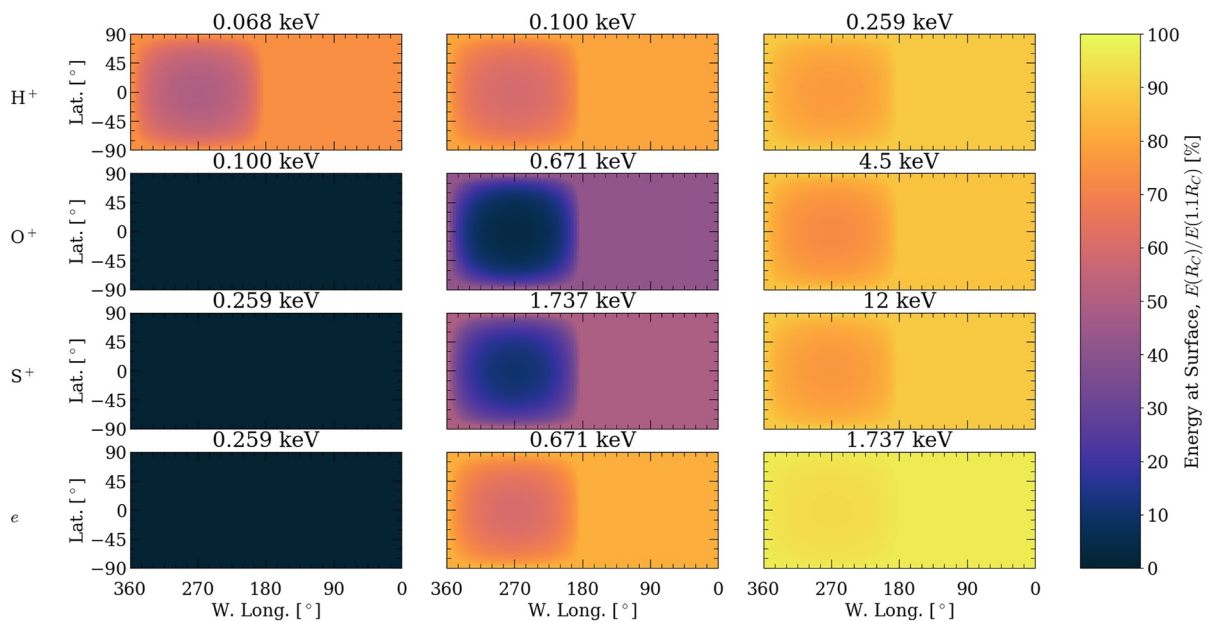


Figure 4. Ratio of energy reaching Callisto's surface, $E(r_C)$, to the energy starting at 1.1 r_C , $E(1.1r_C)$, after calculating energy deposition via Equation 2 in an O₂ atmosphere assuming $n_{0,O_2} = 10^{10}$ cm⁻³ for H⁺ (first row) at $E(1.1r_C) = 0.068$ keV (left subplot), 0.100 keV (middle subplot), and 0.259 keV; for O⁺ (second row) at $E(1.1r_C) = 0.100$ keV (left subplot), 0.671 keV (middle subplot), and 4.5 keV (right subplot); for S⁺ (third row) at $E(1.1r_C) = 0.259$ keV (left subplot), 1.737 keV (middle subplot), 12 keV (right subplot); and for e (fourth row) at $E(1.1r_C) = 0.259$ keV (left subplot), 0.671 keV (middle subplot), and 1.737 keV (right subplot).

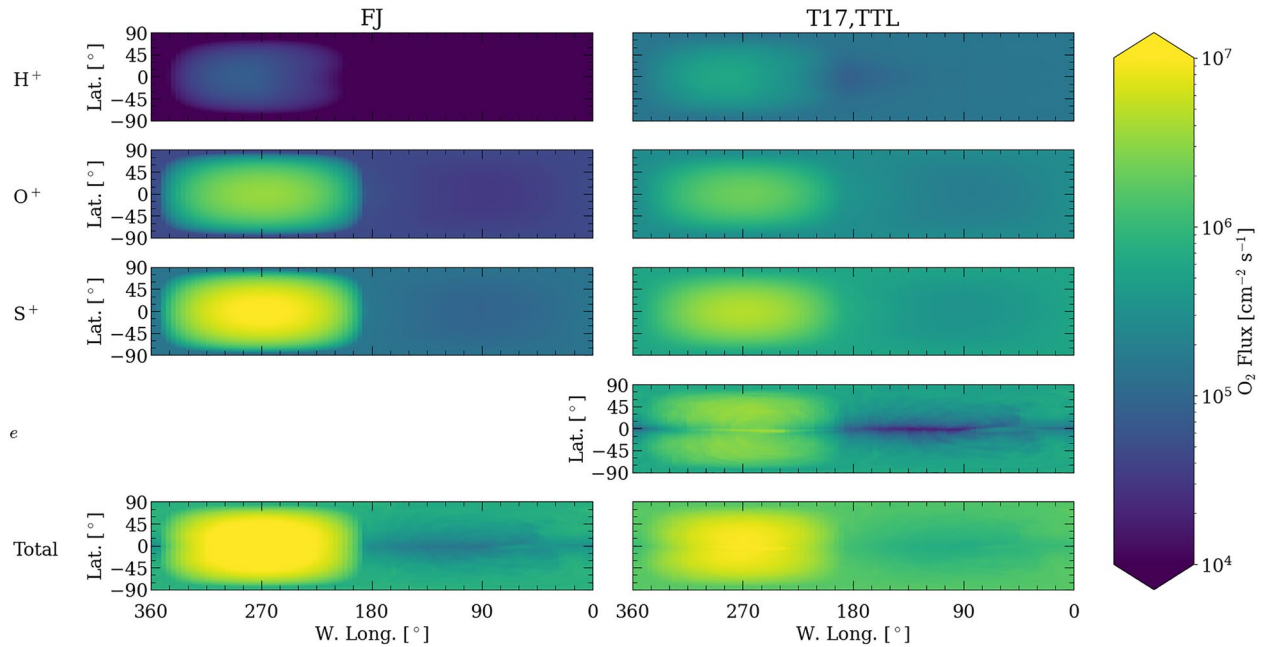


Figure 5. The total flux of O_2 released from Callisto's exposed ice patches by impinging H^+ (first row), O^+ (second row), and S^+ (third row) derived via the FJ (left panels) and TTL (right panels) formulae, and by impinging electrons (fourth row) derived using the original formula and constants from Teolis et al. (2017) as a function of Latitude ("Lat.", y-axes) and W. Longitude ("W. Long.", x-axes) after taking into account energy deposition in an O_2 atmosphere assuming a uniform surface density of $n_{0,O_2} = 10^{10} \text{ cm}^{-3}$. Note the subsolar point is at 0° Lat., 270° W. Long.; and the night-side spans from $-90^\circ \rightarrow +90^\circ$ Lat., $0^\circ \rightarrow 180^\circ$ W. Long.

all of their energy would be deposited in the atmosphere. In such instances, no O_2 is produced at the surface by the O^+ and S^+ ions and electrons of these incident energies. Between these thresholds, energy deposition can still be significant for O^+ and S^+ ; for example, $(E(1.1r_c) = 671 \text{ eV})$ O^+ and $(E(1.1r_c) = 1.737 \text{ keV})$ S^+ ions can deposit almost all of their energies on the day-side hemisphere, with $\sim 50\%$ – 70% of the energy being deposited

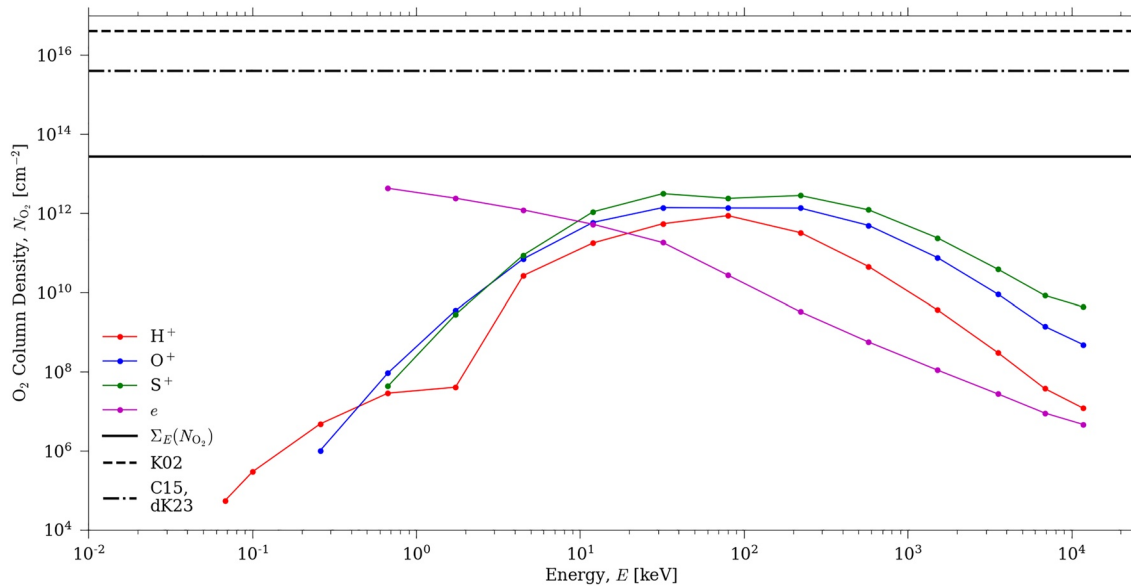


Figure 6. Globally averaged O_2 column densities, N_{O_2} (y-axis), calculated via Equation 4 for H^+ (red line), O^+ (blue line), S^+ (green line), and e (magenta line) across the energy bins considered (x-axis) from $E = 0.034 - 23,596 \text{ keV}$, where the circles represent the energies at the middle of the energy bins. Here the yields are derived according to the TTL and T17 formulae for ions and electrons, respectively. The total N_{O_2} produced across all energy bins and across all the individual plasma components is represented by a solid black line for comparison to N_{O_2} suggested by Kliore et al. (2002) "K02" ($4 \times 10^{16} \text{ cm}^{-2}$, dashed black line) and Cunningham et al. (2015) "C15" and de Kleer et al. (2023) "dK23" ($4 \times 10^{15} \text{ cm}^{-2}$, dash-dotted black line).

on the night-side hemisphere. Energy deposition within the atmosphere is the least significant for protons (due to their relatively small S_n and S_e , see Figure C2 in Appendix C): the most extreme case occurs at 68 eV (the lowest energy considered), where only ~40%–50% of the initial energy is deposited on the day-side atmosphere. Due to the extrapolated values we implement for electrons' S_e below 1 keV, there is a relatively rapid transition from significant energy being deposited in the atmosphere ($E(1.1r_c) \lesssim 259$ eV) to essentially no energy being deposited ($E(1.1r_c) \gtrsim 1.737$ keV), with ~20%–40% being deposited in the atmosphere between these bounds ($E(1.1r_c) = 671$ eV).

We estimate Y_{O_2} and the corresponding flux of O_2 , Φ_{O_2} , at Callisto's surface according to the energies of the plasma fluxes calculated above, where Φ_{O_2} is calculated using the same latitude and longitude coordinates as in GENTOO: a 2° and 4° resolution in latitude and longitude, respectively. The total flux of O_2 produced via radiolysis released from Callisto's surface (Φ_{O_2}) depends on the integral of impinging plasma fluxes (Φ_p) and Y_{O_2} from $E = 0.034 - 23, 596$ keV, as well as the surficial coverage of exposed ice patches in which the O_2 is produced:

$$\Phi_{O_2} = \sum_{p=H^+, O^+, S^+, e} \left[\sum_E \left\{ \Phi_p(E) (Y_{O_2}(E))_p \right\} \right] f_{ice}. \quad (3)$$

Here the subscript p denotes the energy-dependent values for Φ and Y_{O_2} according to the plasma composition: H^+ , O^+ , S^+ , and e ; and $f_{ice} = 10\%$ is the fractional abundance of exposed ice patches (e.g., Carberry Mogan et al., 2022; Spencer, 1987b), for which we assume a uniform distribution throughout the surface. We compare the flux of O_2 produced by the ions based on the formulae used to solve for Y_{O_2} , FJ and TTL, in Figure 5 and Table 1. As can be seen, and as is expected by Y_{O_2} shown in Figure 3, the maximum Φ_{O_2} are larger for O^+ and S^+ when implementing the FJ formula rather than the TTL formula, while Φ_{O_2} for H^+ is larger when implementing the TTL formula rather than the FJ formula. Also, the minimum fluxes, which occur locally on the night-side, for all ion species are larger when implementing TTL formula rather than the FJ formula. The total production rate of O_2 released from the surface for each plasma component is $\sum_{i,j} \Phi_{O_2;i,j} A_{i,j}$, where i and j represent the zenith and azimuthal cells from which Φ_{O_2} and the local surface area, $A_{i,j}$, are calculated. When implementing the FJ formula to solve Y_{O_2} , the production rates induced by the bombarding H^+ , O^+ , and S^+ are $\sim 1.1 \times 10^{22} \text{ s}^{-1}$, $\sim 5.0 \times 10^{23} \text{ s}^{-1}$, and $\sim 1.6 \times 10^{24} \text{ s}^{-1}$, respectively; and when implementing the TTL formula, these rates are $\sim 1.6 \times 10^{23} \text{ s}^{-1}$, $\sim 4.3 \times 10^{23} \text{ s}^{-1}$, and $\sim 8.9 \times 10^{23} \text{ s}^{-1}$, respectively. The total production rate of O_2 released from the surface as a result of the impinging electrons is $\sim 7.0 \times 10^{23} \text{ s}^{-1}$, which is more O_2 released than that via impinging O^+ but less than that via impinging S^+ for either formulae. Thus, when implementing the FJ and TTL formulae to solve Y_{O_2} the total O_2 production rate integrated across all of the plasma composition and energies is $\sim 2.8 \times 10^{24} \text{ s}^{-1}$ and $\sim 2.2 \times 10^{24} \text{ s}^{-1}$, with $H^+:O^+:S^+:e$ ratios of $\sim 0.41:18:57:24$ and $\sim 7.0:20:41:32$, respectively. In either case, S^+ is the primary source of O_2 , but when implementing the TTL formula to solve Y_{O_2} the source of O_2 is more evenly spread among the plasma composition. Further, when solving Y_{O_2} for ions the difference in total O_2 production rates is only a factor of ~ 1.5 more when implementing the FJ formula ($\sim 2.1 \times 10^{24} \text{ s}^{-1}$) relative to that when implementing the TTL formula ($\sim 1.5 \times 10^{24} \text{ s}^{-1}$).

After their initial production via radiolysis, we assume the newly formed O_2 molecules release from the surface, where they supply the atmosphere as follows. These radiolytic products are too heavy and slow to escape the atmosphere, even if they are directly sputtered (e.g., Johnson et al., 1983), especially if they did so into a collisional atmosphere (e.g., Carberry Mogan et al., 2020, 2021, 2022), in which they would thermalize. Further, they are more likely to return to the surface (following either a ballistic trajectory or a path disrupted by collisions) than be dissociated and/or ionized via interactions with solar photons or magnetospheric plasma. On return to the surface, however, they are too volatile to condense and too inert to react with the other surface materials. Instead, they will permeate or become trapped in the porous, radiation-altered regolith and, assuming reactions therein are negligible, eventually thermally desorb back into the atmosphere, where their accumulation is limited by gas-phase ionizing and dissociative processes. Thus, over time, a small ab initio source flux (Figure 5) can eventually lead to a steady-state, global, and even collisional atmosphere, where molecules are continuously returning to and thermally desorbing from the regolith (e.g., Carberry Mogan et al., 2020, 2021, 2022; Johnson et al., 2019).

When determining the O_2 column densities corresponding to the source fluxes estimated above, we only consider photochemical reactions as atmospheric losses (see Table E1 in Appendix E). Although these reactions only occur on the illuminated side of Callisto, as Callisto orbits Jupiter the illumination varies with time. Thus, both

hemispheres of Callisto will be exposed to the Sun throughout the orbit (except in the rare instance when Callisto passes through Jupiter's shadow). Therefore, we reduce the photochemical reactions rates by a factor of 2 to represent each hemisphere spending roughly 1/2 of the orbit illuminated. That is, we implement an average atmospheric lifetime *throughout Callisto's orbit* of $\sim 4.66\text{--}7.80 t_{\text{orb}}$ ($2\times$ that listed in Table E1 in Appendix E), where $t_{\text{orb}} = 1.44 \times 10^6$ s is Callisto's orbital period. In Appendix E, we calculate additional ionization rates corresponding to the plasma fluxes impinging on the atmosphere (Figures E1 and E2). However, these reactions all occur at least an order of magnitude less frequently than do photochemical reactions. Moreover, these rates are calculated according to the plasma fluxes when Callisto is located at the center of the Jovian plasma sheet (Section 3.1), so when averaged over a full synodic period (i.e., also taking into account when Callisto is located above and below the current sheet) they will occur even less frequently. Thus, even taking these additional losses into account, the lifetime is primarily determined according to the photochemical lifetimes (Table E1). Additional loss processes, such as electron impact dissociation of O_2 can be estimated (e.g., using cross-sections from Cosby, 1993) but the result is the same: the lifetimes are negligibly affected, and are primarily determined by the photochemical lifetimes.

Finally, a first-order approximation for an average O_2 column density, N_{O_2} can be calculated assuming there is no O_2 atmospheric escape; that the total O_2 lifetime, τ_{O_2} , is 1/2 those induced via photochemical reactions; and the total Φ_{O_2} released from the exposed ice patches covering 10% of Callisto's surface is the sum of the O_2 fluxes illustrated in Figure 5. The range of N_{O_2} is calculated via the following equation:

$$N_{\text{O}_2} = \tau_{\text{O}_2} \frac{\sum_{i,j} (\Phi_{\text{O}_2,i,j} A_{i,j})}{\sum_{i,j} (A_{i,j})}, \quad (4)$$

where i and j represent the zenith and azimuthal cells from which Φ_{O_2} and the local surface area, $A_{i,j}$, are calculated, which are then averaged over the total surface area of Callisto, $\sum_{i,j} (A_{i,j})$. The O_2 column densities corresponding to the energies of the impinging plasma as well as the total column (integrated across all energies and all plasma components) are illustrated in Figure 6. As can be seen, assuming $\tau_{\text{O}_2} = 6.23 t_{\text{orb}}$ as an average between solar minimum and maximum after being reduced as described above, evaluating Equation 4 gives $N_{\text{O}_2} \sim 3.5 \times 10^{13} \text{ cm}^{-2}$ using the FJ formula and $N_{\text{O}_2} \sim 2.7 \times 10^{13} \text{ cm}^{-2}$ using the TTL formula, both of which are $\sim 2\text{--}3$ orders of magnitude less than that inferred from observations, $\sim 4 \times 10^{15} \text{ cm}^{-2}$ (Cunningham et al., 2015; de Kleer et al., 2023)— $\sim 4 \times 10^{16} \text{ cm}^{-2}$ (Kliore et al., 2002). That is, radiolysis induced by the Jovian magnetospheric plasma in Callisto's exposed ice patches does not produce nearly enough O_2 relative to what has been suggested in Callisto's atmosphere. In Section 5 we discuss ways in which this discrepancy can be resolved.

5. Discussion

Here we discuss the implications of the principal conclusion of this study, that the O_2 atmospheric component produced from Callisto's ice patches via radiolysis is much less dense than what has been inferred from observations. We explore additional sources for O_2 in an attempt to resolve this discrepancy (Section 5.1). In addition, we discuss similar sources for Callisto's H_2 component (Section 5.2).

5.1. Additional Sources of O_2

Because Callisto's interaction with the magnetospheric plasma perturbs the local electromagnetic environment and diverts a large amount of the ambient plasma around the moon (Liuzzo et al., 2022), the fluxes that reach the top of the atmosphere (and potentially, the surface) are much lower than the flux in the ambient plasma. Hence, to confirm that the fluxes of the Jovian plasma are large enough near Callisto's orbit to generate the inferred atmosphere, we investigate the (hypothetical) case where none of the magnetospheric plasma is diverted around the moon; that is, a scenario where Callisto does not perturb the magnetospheric plasma, which then proceeds to impact Callisto's icy surface uninhibited, thereby producing O_2 via radiolysis. We assume the upstream plasma fluxes illustrated in Figure 1 impact Callisto's surface isotropically (but note that since ions below energies $E \lesssim 4$ keV, and electrons below $E \lesssim 2$ MeV, have gyroradii that are below a Callisto radius, they would not precipitate isotropically). In doing so, we find that a much larger O_2 column is produced: $\sim (2\text{--}3) \times 10^{17} \text{ cm}^{-2}$, which is $\sim 1\text{--}2$ orders of magnitude larger than what is inferred from observations. However, since we know that this scenario is only hypothetical (e.g., Liuzzo et al. (2022)), and that radiolysis induced in Callisto's exposed ice

patches is an insufficient source to produce the amount of O₂ inferred from observations, we are left with trying to search for additional mechanisms in which O₂ can be produced at Callisto to resolve this discrepancy.

5.1.1. Callisto's Ice-Rich Surface

Notably, even if we assumed 100% of the surface is covered in ice rather than only 10% (i.e., multiplying the O₂ columns listed in Section 4 by a factor of 10: $\sim(2.7\text{--}3.5) \times 10^{14} \text{ cm}^{-2}$), radiolysis induced in the ice would still be an insufficient source to produce the values inferred from observations.

Since Callisto's surface is sculpted by impacts, a homogeneously mixed ice and non-ice regolith could be created (e.g., Squyres, 1980). Over time, sublimation of ice from such a regolith would deplete the upper layer until the accumulation of the remaining non-ice material, the “lag deposit,” would insulate the underlying ice and inhibit further sublimation. The energetic particles irradiating Callisto's surface can potentially penetrate this non-ice regolith, depending on the initial energies of the impinging charged particles and the thickness of the regolith, producing O₂ (and H₂) in the underlying ice-rich surface; subsequently, these radiolytic products in turn could diffuse through the lag deposit and release into the atmosphere. However, the thickness of this lag deposit is not well constrained. On the one hand, variations in the intensity of emitted thermal infrared (IR) during eclipses were shown to be consistent with a few millimeter ($\sim 10^7 \text{ \AA}$) thick, low-thermal-inertia surface layer of rock powder and/or frost covering a high-thermal-inertia, denser mixture of rock and ice (Morrison & Cruikshank, 1973). Interpretations of radar measurements are also consistent with the description of Callisto's surface being dominated by an ice-rich regolith overlaid by a dark, non-volatile material (Moore et al., 2004 and references therein). On the other hand, the smoothness of much of Callisto's surface on meter-scales as well as the relatively low-albedo bright ray craters suggests a non-ice surface layer on the order of meters ($\sim 10^{10} \text{ \AA}$) thick (Schenk, 1995). Moreover, the thickness of the regolith likely varies locally as a result of geomorphological processes (e.g., Moore et al., 1999; Spencer & Maloney, 1984). Therefore, it is not known what energies are (locally) required for impinging particles to fully penetrate the lag deposit nor what impacting energies will be left over to induce radiolysis in the underlying ice. Further, this is likely only relevant for energetic electrons and, possibly, protons with $E \gtrsim 10 \text{ MeV}$, given their comparatively large penetration depths ($R_p \gtrsim 10^7 \text{ \AA}$; e.g., Figure C1 in Appendix C). However, as electrons with $E \gtrsim 400 \text{ eV}$ penetrate this non-ice or ice-poor material and deposit some energy therein, the corresponding yield can increase, since the yield peaks around this energy (Figure 3). The same can be said for energetic protons with $E > 100 \text{ keV}$, since the yield drops off above this energy, regardless of whether the FJ or TTL formula is used (Figure 3), albeit the drop-off is much sharper in the former. However, the peak number fluxes for these components occur at lower energies, so even if the yields were to increase significantly after high-energy electrons and protons penetrate the non-ice or ice-poor material and impact the underlying ice, this would still likely prove to be an insufficient source of O₂.

Radiolysis in ice could also occur if the dark material, which covers $\sim 90\%$ of the surface is predominantly ice; for example, assuming the ice and non-ice are intimately mixed, with weight fractions as high as 90 wt% (Clark, 1980). However, such a material would have to be an efficient source for radiolytic products but an inefficient source for sublimated H₂O, according to the constraints made by Carberry Mogan et al. (2022): sublimation from this material is (at least) $\times 10^{-3}$ less efficient than that from pure ice. Nevertheless, this still does not produce enough O₂ relative to the constraints inferred from observations: using the FJ and TTL formulae to solve for O₂ yields assuming 90% of the surface is 90 wt% ice with the warm surface temperature distribution from Carberry Mogan et al. (2022), Figure 1a therein, we obtain values of only $\sim 5.4 \times 10^{14} \text{ cm}^{-2}$ and $\sim 3.6 \times 10^{14} \text{ cm}^{-2}$, respectively, which are still $\sim 1\text{--}2$ orders of magnitude lower than the O₂ column densities inferred from observations. Further, the ice fraction on the surface of 90 wt% is an upper bound, with lower estimates of 20%–30% (see discussion in Section 1), hence the O₂ produced in this scenario is likely even lower than these estimates.

5.1.2. Chemical Reactions in Water Vapor

An additional production mechanism for O₂ is through a series of chemical reactions in a water vapor atmosphere. Yung and McElroy (1977) simulated such reactions in a theoretical atmosphere at Ganymede (and suggested the results could be applied to Callisto as well), where water vapor was produced via sublimation and a series of subsequent chemical reactions produced O₂. For example, they considered the reactions $\text{H}_2\text{O} + h\nu \rightarrow \text{H} + \text{OH}$, followed by $\text{O} + \text{OH} \rightarrow \text{O}_2 + \text{H}$ to produce O₂. In their analysis, Yung and McElroy (1977) made the following assumptions. The model was only 1D, and thus neglected the drop-off in local surface temperatures and hence sublimation rates with increasing distance from the subsolar point (Carberry Mogan et al., 2021, 2022).

In addition, the surface was assumed to be “chemically passive” so that the only losses for OH were through collisions ($O + OH \rightarrow O_2 + H$, $OH + OH \rightarrow H_2O + O$), and the losses for O included escape and collisions; that is, they neglected reactions in the surface and photochemical and plasma-induced reactions in the atmosphere for these species.

Although a modern version of the Yung and McElroy (1977) model could be implemented to simulate O_2 production at Callisto, we can apply their findings to obtain a first-order estimate of the contribution from H_2O to the generation of O_2 at Callisto, using numbers consistent with Callisto's H_2O atmosphere. The upper limit for peak H_2O density in Callisto's atmosphere set by Carberry Mogan et al. (2022) is $\sim 10^8 \text{ cm}^{-3}$, which results in a partial H_2O pressure of $\sim 2.3 \times 10^{-9}$ mbar assuming a (subsolar) temperature of ~ 167 K (assuming the ice is intimately mixed with dark material). Note that this pressure is very similar to one of the partial pressures considered by Yung and McElroy (1977): 2.5×10^{-9} mbar (Figures 4 and 5 therein), which they estimated can result in O_2 densities as high as $2 \times 10^{13} \text{ cm}^{-3}$, which is ~ 3 – 4 orders of magnitude larger than what has been inferred from observations ($\sim 10^9$ – 10^{10} cm^{-3} ; Kliore et al., 2002; Cunningham et al., 2015; Carberry Mogan et al., 2022; de Kleer et al., 2023). If, for simplicity, we assume that every H_2O produced becomes OH via dissociative processes, this would result in a maximum OH density of 10^8 cm^{-3} . The primary source of O_2 in Yung and McElroy (1977) then follows from $O + OH \rightarrow O_2 + H$, occurring at a volumetric rate of $5 \times 10^{-11} \text{ cm}^3 \text{ s}^{-1}$. If we then assume that every other OH becomes O via dissociative processes, the maximum density for both O and OH becomes $5 \times 10^7 \text{ cm}^{-3}$. This yields an O_2 production rate of $\sim 2.5 \times 10^{-3} \text{ s}^{-1}$ via O + OH collisions, which is negligible relative to that via radiolysis, which produces on the order of $10^{24} O_2/s$ (see Table 1).

Hence, given the constraints for water vapor at Callisto's subsolar point made by Carberry Mogan et al. (2022), it seems highly unlikely that a sufficient amount of O_2 can be produced via chemical reactions of water vapor in the atmosphere. Further, the constrained H_2O density results in the component being only quasi-collisional near the subsolar point. Therefore, it is not likely that trace species (O and OH) produced via infrequent photochemical reactions could themselves become collisional components in the atmosphere assuming more realistic boundary conditions than in the first-order estimation applied here (e.g., these species would react on their return to the surface). If anything, these trace species would only collide with the more dense, thermal species (O_2 , H_2 , H_2O , and CO_2) in the atmosphere (e.g., Carberry Mogan et al., 2022), but not with each other (e.g., $O + O$, $OH + OH$, $O + OH$ collisions).

5.1.3. Oxygen Ion Implantation

Since oxygen ions are an abundant species in the Jovian magnetosphere at Callisto's distance from Jupiter, oxygen ion implantation in Callisto's non-ice surface material could potentially lead to O_2 production, assuming oxygen ion reacts with other species during penetration of the ice. Hence, analogous to solar wind proton implantation in the lunar regolith leading to H_2 production at the Moon (Stern et al., 2013; Tucker et al., 2019; Wurz et al., 2012), we calculated an upper bound for O_2 production via oxygen ion implantation in the non-ice material. Assuming every 2 implanted oxygen ions neutralize and recombine to produce 1 O_2 (which subsequently releases from the surface) results in a O_2 production rate of $\sim 1.5 \times 10^{23} \text{ s}^{-1}$, which is $\sim 3\times$ less than that via radiolysis in the ice for oxygen ions (Table 1). Thus, this pathway is an insufficient source of O_2 at Callisto as well.

5.1.4. Callisto's Regolith

Johnson and Jesser (1997) described how O_2 can form and subsequently become trapped in porous regolith and/or radiation-damaged ice at Ganymede. Formation and trapping of O_2 has recently been explored at Europa (Johnson et al., 2019). Hence, it is expected that the phenomenon could also occur at Callisto as well. Indeed, O_2 has been observed in Callisto's surface (Spencer & Calvin, 2002).

Analysis of Callisto's surface suggests the predominant non-ice or ice-poor material resembles carbonaceous chondrites (Moore et al., 2004 and references therein). O_2 produced via radiolysis and/or trapped in carbonaceous material has been extensively studied at comets, in particular to explain the surprisingly high abundance of O_2 detected in the coma of comet 67P/Churyumov-Gerasimenko (Luspay-Kuti et al., 2018, 2022; Mousis et al., 2016). Given that similar carbon-bearing species (e.g., CO_2) have been detected in Callisto's surface (Hendrix & Johnson, 2008) and atmosphere (Carlson, 1999), it is possible that O_2 can be produced and trapped in pathways similar to those on comets.

In recent models of Callisto's atmosphere Carberry Mogan et al. (2020, 2021, 2022), it was assumed that the regolith is permeated with O₂ that subsequently is released into and returns from the gas-phase. The source of this O₂ must be reexamined going forward in order to better estimate the O₂ abundance in the atmosphere. We find such processes to be the most compelling as a means to resolve the discrepancy between source rates determined in this study and the suggested abundances. Unfortunately, the data required, such as (local) lateral and vertical composition of Callisto's surface, to conduct a thorough analysis are lacking.

5.2. H₂ Production Constraints

Molecular hydrogen is produced in H₂O-ice via radiolysis concomitantly with molecular oxygen in a stoichiometric ratio of 2:1. Thus, the radiolytic production of H₂ from Callisto's exposed ice patches can be approximated from that for O₂ (Table 1): $\sim(4-6) \times 10^{24}$ H₂/s. Also, as we did for O⁺ implantation in Callisto's non-ice or ice-poor material leading to O₂ production, we can also calculate an upper bound for proton implantation leading to H₂ production: $\sim 2.5 \times 10^{23}$ H₂/s. This is about an order of magnitude larger than H₂ produced by protons via the FJ formula but is about equal to that produced via the TTL formula (after multiplying the O₂ production in Table 1 by a factor of 2). The initial H₂ production rates required by Carberry Mogan et al. (2022) to reproduce the Lyman- α emissions detected by HST are $\sim 0.7-2.3 \times 10^{28}$ H₂/s depending on the primary dissociation mechanisms: photodissociation or magnetospheric electron-impact induced dissociation. Note these production rates are likely over-estimates since additional production of H from Callisto's extended ionosphere (e.g., dissociative recombination of H₃⁺) was not considered and the magnetospheric electron distribution was crudely approximated. Constraining H-production from the former and better approximating the dissociation of H₂ from the latter based on Juno data (Figure 1), both which are the subjects of future work, would likely reduce the required amount of H₂. Indeed, coupling the electron fluxes from Figure 1 with the cross-section data from Scarlett et al. (2018) results in electron impact-induced dissociation rates of H₂ (producing 2H) of $\sim 7.62 \times 10^{-8}$ s⁻¹, which is $\sim 5.9\times$ larger than the rate implemented by Carberry Mogan et al. (2022). Nevertheless, the above estimates for H₂ production from Callisto's exposed ice patches and proton implantation are $\sim 3-5$ orders of magnitude less than that estimated by Carberry Mogan et al. (2022), and are still too small even if we reduce the H₂ production rate according to the updated H-production rate. This discrepancy is larger than that discussed earlier for O₂, because H₂ does thermally escape from Callisto's atmosphere, and thus a larger source is required to compensate for this additional sink. This suggests that H₂, like O₂, must be produced in Callisto's regolith, which is plausible given that the presence of H₂S (Cartwright et al., 2020), hydrocarbons (McCord et al., 1997, 1998), and carbonic acid (Johnson et al., 2004) has been suggested in Callisto's surface, from which H₂ can be produced via radiolysis.

6. Conclusion

Using state-of-the-art models to simulate Callisto's local plasma environment coupled with an energy deposition model as well as radiolytic production yield estimates based on extensive laboratory data, we have shown that radiolysis induced only in Callisto's exposed ice patches by the Jovian magnetospheric plasma does not produce sufficient O₂ to account for the column densities inferred from observations of Callisto's atmosphere (Cunningham et al., 2015; de Kleer et al., 2023; Kliore et al., 2002). Since O₂ does not (thermally) escape, losses in the gas-phase (e.g., Table E1) primarily limit its atmospheric enrichment. Therefore, these steady-state densities can only come about if there are additional sources. Having examined a number of additional sources (Section 5.1), we suggest that the upward flux of O₂ from the regolith principally supplies the inferred atmospheric column. O₂ can accumulate in Callisto's porous regolith as a result of being weakly bound to defect sites on grain surfaces, as suggested to account for Europa's dusk/dawn asymmetry (Johnson et al., 2019); being stably trapped in bubbles in grains (e.g., Johnson & Jessor, 1997), consistent with observations of O₂ on Callisto's surface (Spencer & Calvin, 2002); and/or being recycled therein via reactions (e.g., Shematovich, 2006; Shematovich & Johnson, 2001; Shematovich et al., 2005). Therefore, a better understanding of the production and fate of the O₂ in the regolith is required in order to place better constraints on the mechanisms for generating Callisto's O₂ atmosphere. Indeed, this aspect is of considerable interest in preparation for the upcoming missions to the Jovian system.

During the *Galileo* mission, large electron densities were detected within ~ 50 km of Callisto's surface, which were used to infer O_2 surface densities of 10^{10} cm^{-3} (Kliore et al., 2002). More recently, observations of the moon's atmosphere suggest O_2 densities that are an order of magnitude lower (Cunningham et al., 2015; de Kleer et al., 2023). Since these measurements were taken across nearly two decades by three separate instruments each using distinct measurement techniques, it is not possible to determine whether the variability in these observations is due to changes in Callisto's atmosphere that occur over multi-year timescales, or is instead generated by some other mechanism including, for example, variability in ionospheric pickup and outflow driven by the moon's plasma interaction (Liuzzo et al., 2015, 2016). Indeed, Callisto's ambient magnetospheric environment is highly variable (over minutes-to-hours from, e.g., the synodic rotation of Jupiter, but also potentially over decades-long timescales); hence, the mechanisms responsible for generating the moon's atmosphere are themselves likely variable. Also, all of these observations required some sort of model to interpret the data, and the discrepancies in the inferred densities could stem from the assumptions implemented in those models. Regardless, for future targeted encounters (e.g., during the JUICE mission), it is imperative to obtain multi-point, concurrent measurements of the moon's charged and neutral particle environments in order to further constrain the mechanisms responsible for generating Callisto's observed neutral envelope.

Appendix A: Callisto's Ambient Plasma Environment

Figure 1 displays the ambient differential flux of protons, oxygen, sulfur, and electrons near Callisto's position within the Jovian magnetosphere. For energetic ions (blue lines in panels 1a–c), the modeled spectra are based on observations from the *Galileo* mission at times when the probe was located near Callisto's orbital position (but far from the moon itself) and within the center of the Jovian plasma sheet. Dashed segments of these lines represent energies at which these fits have been extrapolated, since the *Galileo* Energetic Particle Detector was not able to detect particles at those energies (see also Cooper et al., 2001; Mauk et al., 2004). The energetic electron spectra (blue lines in panel 1d) are obtained from the *Galileo* Interim Radiation Electron (GIRE) model (Garrett et al., 2003) for electrons at energies $E > 32$ keV, and from a “transition” kappa distribution for electrons (orange curve) at energies $4.5 \text{ keV} \leq E \leq 32 \text{ keV}$ (see discussion in Jun et al., 2019). In addition to these fits, *Juno* observations from the Jupiter Energetic-Particle Detector Instrument (JEDI) instrument (Mauk et al., 2017) are included as green dots in Figure 1. These observations were taken when the spacecraft was located near Callisto's orbital position of $26r_J$ and was embedded within the center of the current sheet. Further discussion of these fits and the *Juno* energetic measurements can be found in Liuzzo et al. (2022).

Besides the curves and *Juno* observations for the energetic particles, Figure 1 also extends to lower energies, for which we assume a Maxwellian distribution of the plasma. For ions, we use temperatures $k_B T_i = 10$ keV, where k_B is the Boltzmann constant, as observed by *Juno* and reported in Kim et al. (2020), and a total ion density of $n_i = 0.08 \text{ cm}^{-3}$, which is consistent with the plasma density when Callisto is located near the center of the Jovian magnetospheric current sheet (see also Kivelson et al., 2004). We assume the magnetospheric ions are singly charged, and partition the resulting distribution according to the relative abundance of protons, oxygen ions, and sulfur ions in the magnetospheric plasma near Callisto's orbit (see Figure 9 in Kim et al., 2020), corresponding to an ion composition of 14% hydrogen, 37% oxygen, and 47% sulfur (for all charge states). For electrons, we use a temperature of $k_B T_e = 40$ eV and density of $n_e = 0.09 \text{ cm}^{-3}$ (see, e.g., Kivelson et al., 2004; Jun et al., 2019). In addition, example observations of typical thermal populations from the *Juno* Jovian Auroral Distributions Experiment (JADE) instrument (McComas et al., 2017) have been included in Figure 1 as red dots. These observations are calculated from the JADE level 3 low-rate science count rate products in the time range of 2018–248 13:00 to 14:00. For ions, this range is identical to the time for which Liuzzo et al. (2022) presented the JEDI (energetic) particle observations (see green points in Figure 1a–1c). Error bars are also included, given by the uncertainties from Poisson counting statistics and time-dependent background subtraction summed in quadrature over all look directions (Wilson, 2022).

As can be seen in Figure 1, the Juno measurements agree well with the fits of differential particle flux used for this study. For energetic ions, the JEDI observations are nearly perfectly overlain with the analytical expression from Mauk et al. (2004), while for energetic electrons, there is a factor of ~ 2 enhancement in the measurements compared to the GIRE model. At lower energies, the Juno measurements again agree well with the analytical fits. Notably for protons, Juno JADE detected a higher differential flux from energies $1 \text{ keV} \leq E \leq 4 \text{ keV}$ than predicted by the Maxwellian (using parameters from Kim et al., 2020) and power-law (using parameters from Mauk et al., 2004) fits. This could be explained as a variability in Callisto's magnetospheric environment when near the center of the Jovian plasma sheet, as the JADE observation is from a single point in time. Note that since Kim et al. (2020) apply a more statistical approach, we apply their fits (yellow curves in Figure 1) to characterize Callisto's thermal plasma environment.

Appendix B: Temperature Distribution for Callisto's Exposed Ice Patches

Assuming a constant albedo for the ice (a_{ice}), unit emissivity, and that the temperature gradient is axisymmetric about the subsolar point, the radiative equilibrium equation

$$\sigma T_{\text{ice}}^4(\chi) = (1 - a_{\text{ice}})F \cos(\chi) \quad (\text{B1})$$

can be re-arranged to solve for T_{ice} and integrated across the day-side ($0^\circ \leq \chi < 90^\circ$) hemisphere:

$$\int_{0^\circ}^{90^\circ} \{T_{\text{ice}}(\chi)\} \sin(\chi) d\chi = \int_{0^\circ}^{90^\circ} \left\{ \left(\frac{(1 - a_{\text{ice}})F \cos(\chi)}{\sigma} \right)^{1/4} \right\} \sin(\chi) d\chi, \quad (\text{B2})$$

resulting in the following equation:

$$\langle T_{\text{ice}} \rangle = \left(\frac{(1 - a_{\text{ice}})F}{\sigma} \right)^{1/4} \int_{0^\circ}^{90^\circ} \sin(\chi) \cos^{1/4}(\chi) d\chi = \frac{4}{5} \left(\frac{(1 - a_{\text{ice}})F}{\sigma} \right)^{1/4}. \quad (\text{B3})$$

Here χ is the solar zenith angle; T_{ice} is the local temperature of the ice patches; the brackets represent an average over Callisto's day-side hemisphere; σ is the Stefan-Boltzmann constant; and F is the average solar flux (1360.8 W m^{-2}) scaled to 5.2 AU, the average distance of the Jovian system from the Sun. Applying the disk-averaged ice temperatures at Callisto derived by Grundy et al. (1999) of $\sim 115 \text{ K}$ as $\langle T_{\text{ice}} \rangle$, we can solve for the ice albedo by re-arranging Equation B3:

$$a_{\text{ice}} = 1 - \frac{\sigma((5/4)\langle T_{\text{ice}} \rangle)^4}{F} \sim 0.51. \quad (\text{B4})$$

Having obtained the average albedo of Callisto's ice patches, and assuming it is approximately uniform across the surface, we can calculate a day-side temperature distribution for the ice patches, by plugging $a_{\text{ice}} \sim 0.51$ back into Equation B1.

Appendix C: Irradiation of Callisto's Surface and Atmosphere

As the charged particles comprising the Jovian magnetospheric plasma penetrate Callisto's atmosphere, non-thermal energy can be deposited via collisions and neutral particles can be dissociated and/or ionized. If the plasma can penetrate the atmosphere without depositing all of its energy therein, it will then impact and penetrate Callisto's icy surface, thereby producing O_2 via radiolysis. To calculate O_2 yields for the energetic particles irradiating Callisto's icy surface using the formulae of Famá et al. (2008) and Johnson et al. (2009) in Section 3.4 as well as the energy deposition and energetic particle impact ionization rates in Callisto's O_2 atmosphere in Sections 3.3 and Appendix E, respectively, we first derive energy-dependent stopping cross-sections, S , in solid H_2O -ice (Figure C1a) and gas-phase O_2 (Figure C2a).

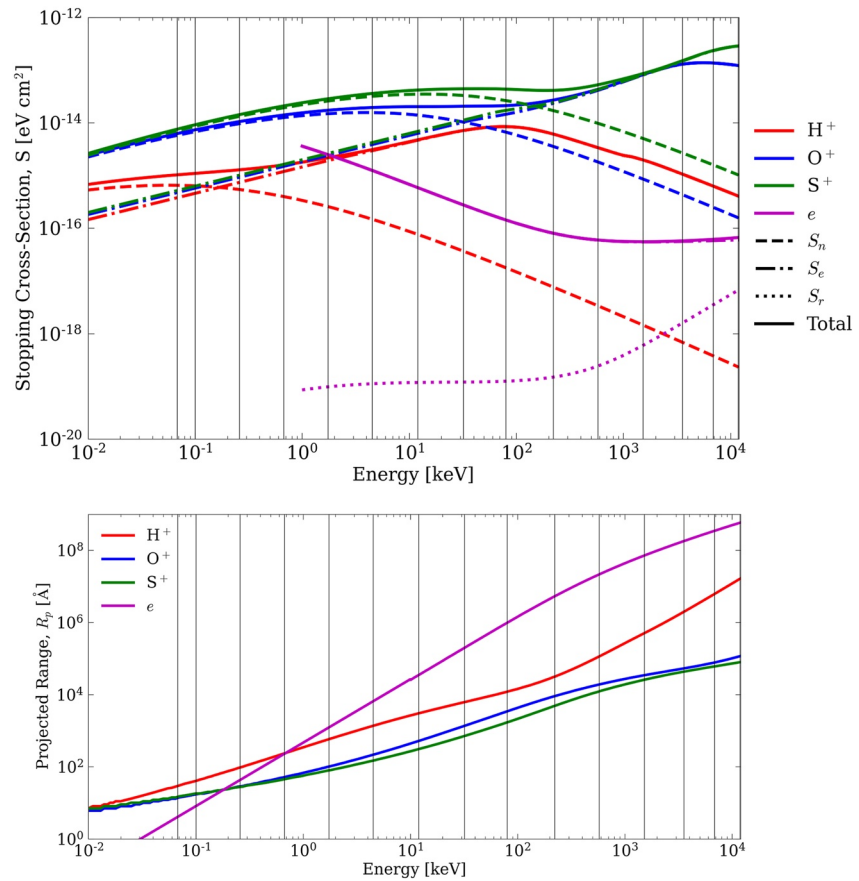


Figure C1. (a) Stopping cross-sections in solid H₂O-ice, S , calculated over an energy range of $10 \text{ eV} \leq E \leq 12 \text{ MeV}$ for H⁺ (red lines), O⁺ (blue lines), S⁺ (green lines), and electrons (magenta lines). Transport of Ions in Matter (TRIM) is used to calculate nuclear and electronic stopping cross-sections, S_n (dashed lines) and S_e (dash-dotted lines), respectively, for the ions; and ESTAR is used to calculate S_e and radiative stopping cross-section, S_r (dotted line), for the electrons. The total stopping cross-section (solid lines) is the sum of S_n and S_e for the ions and the sum of S_e and S_r for the electrons. Note that since $S_e \gg S_n$ for H⁺ above $\sim 1 \text{ keV}$ and S_r is negligible over the entire energy range considered, the dash-dotted and solid red lines as well as the dashed and solid magenta lines essentially coincide over most of the presented energy range. Also, ESTAR only simulates $E \geq 1 \text{ keV}$, hence why the magenta lines start from that energy. (b) Projected ranges, R_p , calculated over the same energy range as (a) via TRIM for H⁺ (red line), O⁺ (blue line), and S⁺ (green line) impacting solid H₂O-ice. For electrons (magenta line) with $E < 10 \text{ keV}$ $R_p = R_0(E/1 \text{ keV})^a$, where $R_0 = 46 \text{ nm}$ and $a = 1.76$ assuming a target (mass) density of 1 g/cm^3 (Johnson, 1990 and references therein) and with $10 \text{ keV} \leq E \leq 12 \text{ MeV}$ R_p is equal to the CSDA-range calculated via ESTAR, hence the slight discontinuity at 10 keV . The individual energy bins from which the plasma fluxes are obtained (see Section 3.1) are illustrated by vertical black lines in both (a) and (b).

We utilize the commercial software Transport of Ions in Matter (TRIM) (Ziegler & Biersack, 1985) to calculate nuclear and electronic stopping cross-sections, S_n and S_e , respectively, for hydrogen, oxygen, and sulfur ions, and Stopping Powers and Ranges for Electrons (ESTAR) (Berger, 1995) to calculate S_e and radiative stopping cross-section, S_r , for electrons. These stopping cross-sections are used to determine the corresponding stopping powers, or the average rate of projectile energy loss per unit path length into a target material with density, n : the nuclear stopping power, $(dE/dx)_n = nS_n$, is due to the transfer of energy to recoiling atoms in elastic collisions; the electronic stopping power, $(dE/dx)_e = nS_e$, is due to Coulomb collisions resulting in the ionization and excitation of atoms; and the radiative stopping power, $(dE/dx)_r = nS_r$, is due to collisions with atoms and atomic electrons in which bremsstrahlung quanta are emitted, which is only important for electrons, but, as seen in Figures C1a and C2a, is negligible over the energies considered. The total stopping cross-sections shown in Figures C1a and C2a are the sums of S_n and S_e for the ions and the sum of S_e and S_r for the electrons. Note that, unlike GENTOO (Section 3.1), TRIM does not differentiate between charges of the ions. However, this is not expected to affect our results.

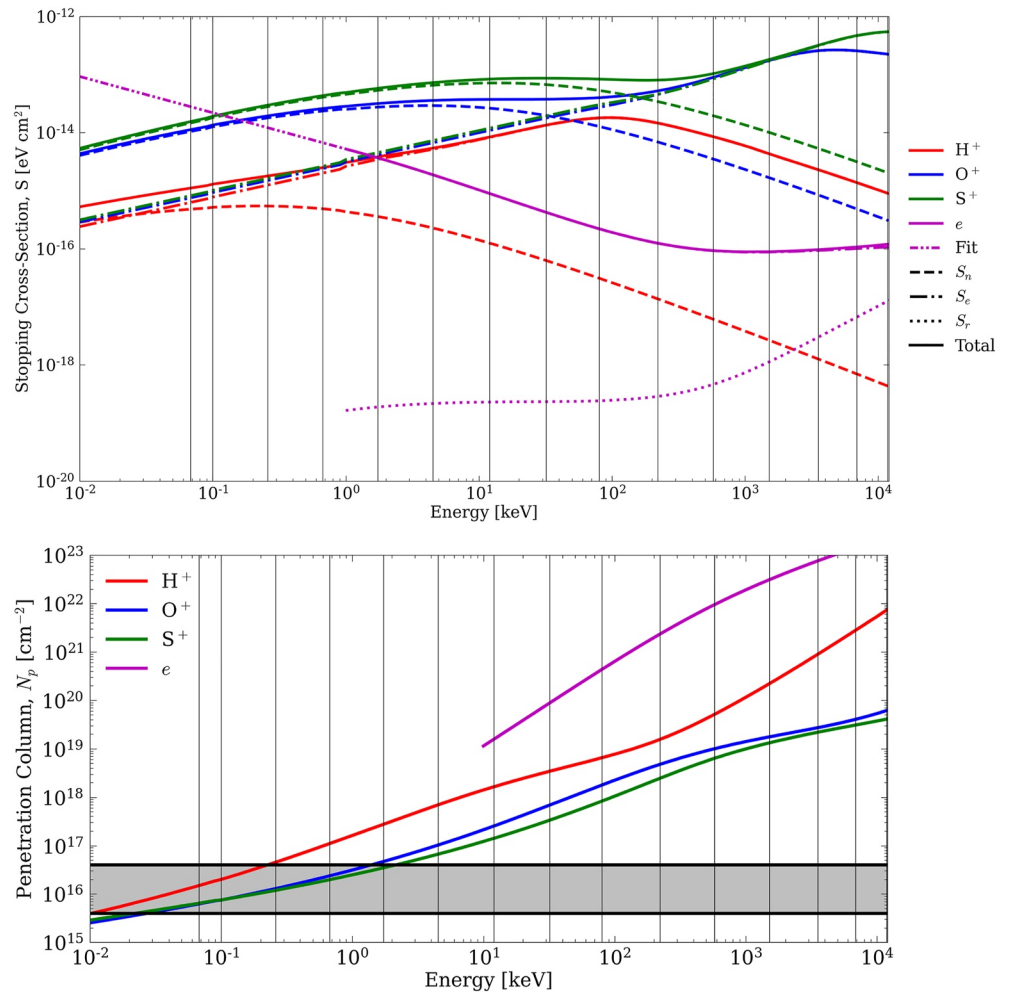


Figure C2. (a) Stopping cross-sections in gas-phase O₂, S , calculated over an energy range of 10 eV $\leq E \leq$ 12 MeV for H⁺ (red lines), O⁺ (blue lines), S⁺ (green lines), and electrons (magenta lines). Transport of Ions in Matter (TRIM) is used to calculate nuclear and electronic stopping cross-sections, S_n (dashed lines) and S_e (dash-dotted lines), respectively, for the ions; and ESTAR is used to calculate S_e and radiative stopping cross-section, S_r (dotted line), for the electrons. The total stopping cross-section (solid lines) is the sum of S_n and S_e for the ions and the sum of S_e and S_r for the electrons. Due to the lack of data for S_e for electrons penetrating an O₂ gas below 1 keV, we extrapolate the slope of S_e between 1 and 1.5 keV and apply that for $E < 1$ keV. This is labeled as “Fit” and is represented by a dash-double-dotted magenta line. (b) Penetration columns, N_p , calculated over the same energy range as (a) via TRIM for H⁺ (red line), O⁺ (blue line), and S⁺ (green line) and via ESTAR for electrons (magenta line) impacting gas-phase O₂. Note N_p is calculated by multiplying the projected range, R_p , by the number density assumed in the TRIM simulation, which for gas-phase O₂ is 5.4×10^{19} cm⁻³. To calculate N_p via ESTAR gas-phase O₂ with the same density as that in TRIM is manually entered for the target material, and the resultant CSDA-range, which can only be calculated for $E \geq 10$ keV, is multiplied by the density. The range of column densities inferred from observations are shaded in black with the lower and upper black lines set at 4×10^{15} cm⁻² (Cunningham et al., 2015; de Kleer et al., 2023) and 4×10^{16} cm⁻² (Kliore et al., 2002), respectively. The individual energy bins from which the plasma fluxes are obtained (see Section 3.1) are illustrated by vertical black lines in both (a) and (b).

We also used TRIM to estimate the projected ranges, R_p , of the impinging ions into H₂O-ice measured parallel to the ions' incident directions (Figure C1b); that is, R_p is the average depth to which the ions will penetrate the H₂O-ice in the course of slowing down to rest. These are used when calculating sputtering yields via the formula of Teolis et al. (2017) as described in Section 3.4. Since electrons are readily scattered upon penetration of H₂O-ice, their R_p can be much larger than the heavier ions. While TRIM only simulates *ions* penetrating a target material and the concomitant R_p , ESTAR can give estimates for the continuous-slowing-down approximation (CSDA) range for penetrating electrons. For fast and heavy penetrating ions (e.g., energetic O⁺ and S⁺) there

is significant forward momentum so that the CSDA-range is only slightly different from R_p . Since electrons are so readily scattered, these values can be significantly different such that the CSDA-range is $\gg R_p$. Nevertheless, for lack of a better formula or experimental data for electrons above ~ 10 keV, we implement the CSDA-range calculated via ESTAR as the electrons' R_p . Below this energy, however, we implement the analytic equation typically applied for keV electrons assuming a target (mass) density of 1 g/cm^3 (e.g., Johnson, 1990 and references therein): $R_p \sim 460 \text{ \AA} (E/1\text{keV})^{1.76}$.

The penetration columns, N_p , calculated over an energy range of $10 \text{ eV} \leq E \leq 12 \text{ MeV}$ for H^+ , O^+ , S^+ , and e impacting gas-phase O_2 are also presented in Figure C2b. N_p is similar to R_p , in that it is the average column density of a gas in which the impinging particles will penetrate in the course of slowing down to rest. Indeed, N_p is the product of R_p and the simulated density of the gas, which is $5.4 \times 10^{19} \text{ cm}^{-3}$ for gas-phase O_2 in TRIM, which we manually set as the target material (gas-phase O_2) density in ESTAR. As shown in Figure C2b, above 10 keV all of the considered charged particles' N_p are more dense than the largest O_2 column density inferred from observations, $\sim 4 \times 10^{16} \text{ cm}^{-2}$ (Kliore et al., 2002). As a result, such particles will be able to successfully penetrate even the most dense O_2 column at Callisto without depositing all of their energy therein, and will subsequently impact the underlying surface. However, as discussed in Section 3.3 and also shown in Figure C2b, within the range of column densities inferred from observations, $4 \times 10^{15} \text{ cm}^{-2}$ (Cunningham et al., 2015; de Kleer et al., 2023)— $4 \times 10^{16} \text{ cm}^{-2}$ (Kliore et al., 2002), thermal ($E \lesssim 1 \text{ keV}$) H^+ , O^+ , and S^+ will deposit a non-negligible amount, if not all, of their energy within the O_2 atmospheric component, thereby diminishing sputter and radiolytic production yields or altogether inhibiting sputtering of the underlying surface.

Appendix D: Radiolytic Production of O_2 in Callisto's Exposed Ice Patches

To calculate Y_{O_2} for impinging ions via the FJ formula, we first calculate the temperature-independent yield for H_2O sputtered from ice, $Y_{\text{H}_2\text{O}}$, which is written as the following:

$$Y_{\text{H}_2\text{O}} = (Y_n + Y_e) \cos^{-f}(\vartheta). \quad (\text{D1})$$

Here Y_n and Y_e are the nuclear and electronic sputtering yields of H_2O , respectively; $f = 1.3 \left(1 + \frac{\ln(m_{\text{ion}})}{10}\right)$ (Famá et al., 2008) is a fit parameter according to the mass of the impinging ion, m_{ion} ; and ϑ is the macroscopic incidence angle of the impinging plasma, which we assume is 45° .

Cassidy et al. (2013) showed that the formula from Johnson et al. (2009) fit better to experimental sputtering data than the formula from Famá et al. (2008) for energies above $\sim 10^2$ keV, where electronic sputtering dominates. Therefore, we neglect the terms in the original formula of Famá et al. (2008) which were used to estimate Y_e as a function of the electronic stopping cross-section squared, S_e^2 , and instead use the formula from Johnson et al. (2009) to solve for Y_e . However, to calculate Y_n we implement the same nuclear stopping cross-section, S_n -dependent portion of the formula from Famá et al. (2008):

$$Y_n = \frac{3\alpha S_n}{4\pi^2 C_0 U_0}. \quad (\text{D2})$$

Here $\alpha = 0.25574 + 1.25338 \exp(-0.86971 m_{\text{ion}}) + 0.3793 \exp(-0.10508 m_{\text{ion}})$ is a fit parameter; $C_0 = 1.3 \text{ \AA}$ is the constant of the differential cross section for elastic scattering in the binary collision approximation; and $U_0 = 0.45 \text{ eV}$ is the surface-binding energy for H_2O .

Using the formula of Johnson et al. (2009) we calculate Y_e as:

$$Y_e = \frac{1}{1/Y_{\text{low}} + 1/Y_{\text{high}}}. \quad (\text{D3})$$

Here Y_{low} and Y_{high} are fits in two different regimes of ion energies, both of which can be expressed as $Z^{2.8} C_1 \left(\frac{v/v_e}{Z^{1/3}}\right)^{C_2}$ with $C_1 = 4.2$ and $C_2 = 2.16$ for Y_{low} and $C_1 = 11.22$ and $C_2 = -2.24$ for Y_{high} ; v/v_e is speed of the impinging ion, v , divided by the speed of a ground-state electron in the Bohr hydrogen model, $v_e = 2.19 \times 10^6 \text{ m/s}$; and Z is the atomic number of the ion.

Famá et al. (2008) calculate a *total* yield of water-mass products (H_2O and $\text{H}_2 + 1/2 \text{O}_2$) by multiplying Equation D1 by a factor of $\left(1 + \beta \exp\left(-\frac{E_a}{k_B T_0}\right)\right)$, where $\beta = 220$ is a fit to experimental data; $E_a = 0.06$ eV is the activation energy which determines the temperature dependence of the decomposition of H_2O molecules; and T_0 is the local surface temperature of the exposed ice patches (Figure 2). We attribute the temperature dependence of that equation to the thermally activated processes leading to the radiolytic production of O_2 ; that is,

$$(Y_{\text{O}_2})_{\text{ion,FJ}} = Y_{\text{H}_2\text{O}} \left(\beta \exp\left(-\frac{E_a}{k_B T_0}\right) \right). \quad (\text{D4})$$

The yields derived by Teolis et al. (2017) are different from those derived via the FJ formula because the former suggests that penetrating projectiles become less efficient at producing O_2 with increasing R_p . Teolis et al. (2017) suggested this inverse projectile-range dependence in the O_2 yields below a surface layer \sim tens of Å thick is a result of oxygenated species not surviving long enough to diffuse through the ice to the surface, and instead reacting with H and H_2 . Above this layer, however, since the near-surface hydrogen atoms and molecules more readily diffuse through or are directly sputtered from the ice, the O_2 becomes enriched due to a lack of chemical destruction pathways. Thus, highly penetrating energetic ions tend to be less efficient at producing O_2 than slower and/or heavier ions which deposit most of their energy near the surface. Teolis et al. (2017) therefore derives Y_{O_2} via the following equation:

$$(Y_{\text{O}_2})_{\text{ion,TTL}} = g_0 E \left(\frac{x_0}{R_p \cos(\theta)} \right) \left(1 + q_{\text{O}_2} \exp\left(-\frac{Q}{k_B T_0}\right) \right) \left[1 - \exp\left(-\frac{R_p \cos(\theta)}{x_0}\right) \right]. \quad (\text{D5})$$

Here $q_{\text{O}_2} = 1000$ is a fit parameter from Teolis et al. (2017) used to describe the exponential temperature dependence; and the other values are taken from Tribbett and Loeffler (2021), who made an empirical correction to the original formula to improve the fits to the data: $g_0 = 10^{-3}$ is the surface radiolysis yield of O_2 , $x_0 = 90$ Å is the suggested thickness of the surface layer where O_2 production is efficient, and $Q = 0.07$ eV is related to the effective activation energy.

To determine Y_{O_2} for the penetrating electrons we apply Equation D5 with the original constants given in Teolis et al. (2017): $g_0 = 5 \times 10^{-3}$, $x_0 = 30$ Å, and $Q = 0.06$ eV. Hence Y_{O_2} for electrons is labeled with “T17” in Figure 3. Note we do not implement a reduction factor to the derived Y_{O_2} as suggested by others (Davis et al., 2021: 0.25; Meier & Loeffler, 2020; Teolis et al., 2017: 0.3), as it remains unclear whether this value, which was used to better match theoretical to experimental results, is a result of measurement and/or model error. Since electrons are more readily scattered than ions upon penetration of H_2O -ice, their R_p can be much larger. Therefore, we implement the CSDA-range, which is a close approximation to the total path length traveled by a charged particle as it slows down to rest, as the electrons' R_p above 10 keV (see Appendix C). Below this energy, we implement the analytic equation typically applied for keV electrons assuming a target (mass) density of 1 g/cm^3 (e.g., Johnson, 1990 and references therein): $R_p \sim 460 \text{ Å} \left(\frac{E}{1 \text{ keV}} \right)^{1.76}$.

Appendix E: Atmospheric Loss Rates

Table E1 lists the rates for these photochemical reactions corresponding to solar activity (minimum–maximum) as well as the total photochemical lifetime for O_2 .

Figure E1 illustrates the thermal ($E \lesssim 4.5$ keV) electron impact ionization rates across Callisto's atmosphere at $1.1 r_c$. These are calculated using the fit from Carberry Mogan, Johnson, et al. (2023) for electron impact ionization cross-sections multiplied by the local electron fluxes. Note that these local electron impact ionization rates can increase with depth into the atmosphere in the instances when $E(1.1r_c) > 100$ eV and some energy is deposited along the trajectory to the surface because the peak in the cross-section distribution occurs around $E \sim 100$ eV.

Table E1
Photochemical Reactions in Callisto's O₂ Atmosphere

Reaction	Rate ^a [s ⁻¹]	Total lifetime ^b [<i>t</i> _{orb} ^c]
O ₂ + hν → O(³ P) + O(¹ D)	(1.50–2.30) × 10 ⁻⁷	2.33–3.90
O ₂ + hν → O ₂ ⁺ + e	(1.73–4.36) × 10 ⁻⁸	
O ₂ + hν → O ⁺ + O + e	(0.407–1.28) × 10 ⁻⁸	
O ₂ + hν → O(³ P) + O(³ P)	(5.36–7.95) × 10 ⁻⁹	
O ₂ + hν → O(¹ S) + O(¹ S)	(1.44–3.46) × 10 ⁻⁹	

^aRange of values are for a “quiet” Sun (i.e., solar minimum) to an “active” Sun (i.e., solar maximum) (Huebner & Mukherjee, 2015) scaled to 5.2 AU. ^bTotal lifetime is estimated as the inverse of the sum of the photochemical reaction rates. ^cCallisto's orbital period, *t*_{orb} = 1.44 × 10⁶ s.

Figure E2 illustrates the thermal and energetic ion- and energetic (*E* > 4.5 keV) electron-impact ionization rates. These rates are determined locally for each plasma component (_{*p*}) in each zenith and azimuth cell via the following equation:

$$\frac{\sum_E (\Phi(E) S_e(E))_p}{W_e} \quad (\text{E1})$$

where *W_e* = 31 eV is the average energy expended by the incident charged particles that goes into ionization of O₂ molecules (Johnson, 1990). Similar to the thermal electron-impact ionization rates, these local energetic particle-impact ionization rates can increase with depth into the atmosphere when energy is deposited along the trajectory to the surface and *S_e* increases as a function of the reduced energy.

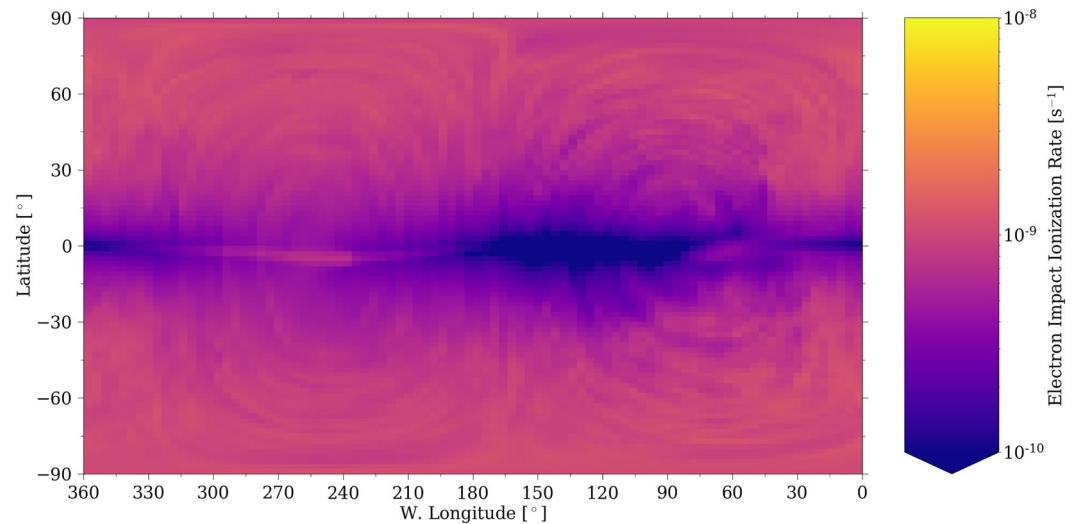


Figure E1. Thermal (*E* ≤ 4.5 keV) electron impact ionization rates calculated at 1.1 *r_c* (color bar) as a function of Latitude (*y*-axis) and W. Longitude (*x*-axis). Note the subsolar point is at 0° Latitude, 270° W. Longitude; and the night-side spans from −90° → +90° Latitude, 0° → 180° W. Longitude.

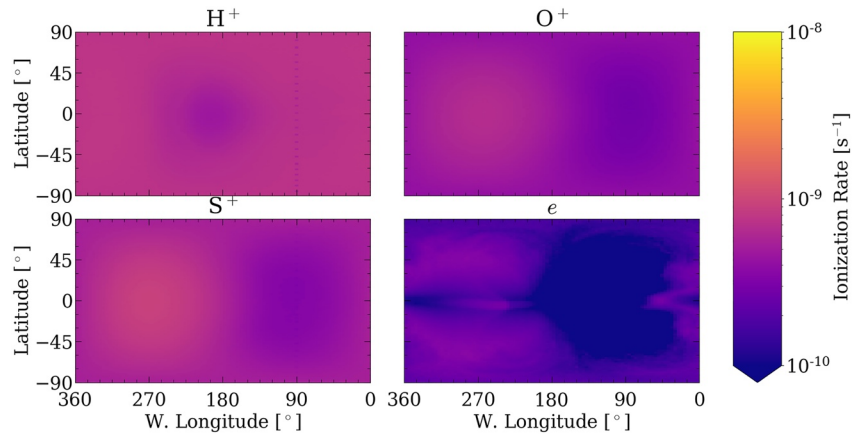


Figure E2. Charged particle impact ionization rates calculated via Equation E1 in Callisto's O₂ atmosphere (ignoring any attenuation) as a function of Latitude (y-axis) and W. Longitude (x-axis) for impinging H⁺ (top-left panel), O⁺ (top-right panel), S⁺ (bottom-left panel), and electrons (bottom-right panel). For electrons, ionization rates are only calculated via Equation E1 for energies above 4.5 keV; at and below this energy, the ionization rates are calculated according to the electron impact ionization cross-sections of (Carberry Mogan, Johnson, et al., 2023) and the local electron fluxes as illustrated in Figure E1. Note the subsolar point is at 0° Latitude, 270° W. Longitude; and the night-side spans from -90° → +90° Latitude, 0° → 180° W. Longitude.

Appendix F: Results for an O₂ Atmosphere with a Prescribed Uniform Surface Density of $n_0 = 10^9 \text{ cm}^{-3}$

Here we present the same results as those presented in Section 4 but the implemented uniform surface density of the O₂ atmosphere is $n_{0,O_2} = 10^9 \text{ cm}^{-3}$ (rather than $n_{0,O_2} = 10^{10} \text{ cm}^{-3}$). Figure 4 illustrates several instances of energy deposition in Callisto's O₂ atmosphere by comparing the energy of the fluxes at the surface, $1 r_C$, compared to that at the top of the atmosphere at $1.1 r_C$ Figure F1. Next, we compare the flux of O₂ produced by the ions based on the formulae used to solve for Y_{O_2} , FJ and TTL, in Figure F2 and Table F1. Finally, the O₂ column

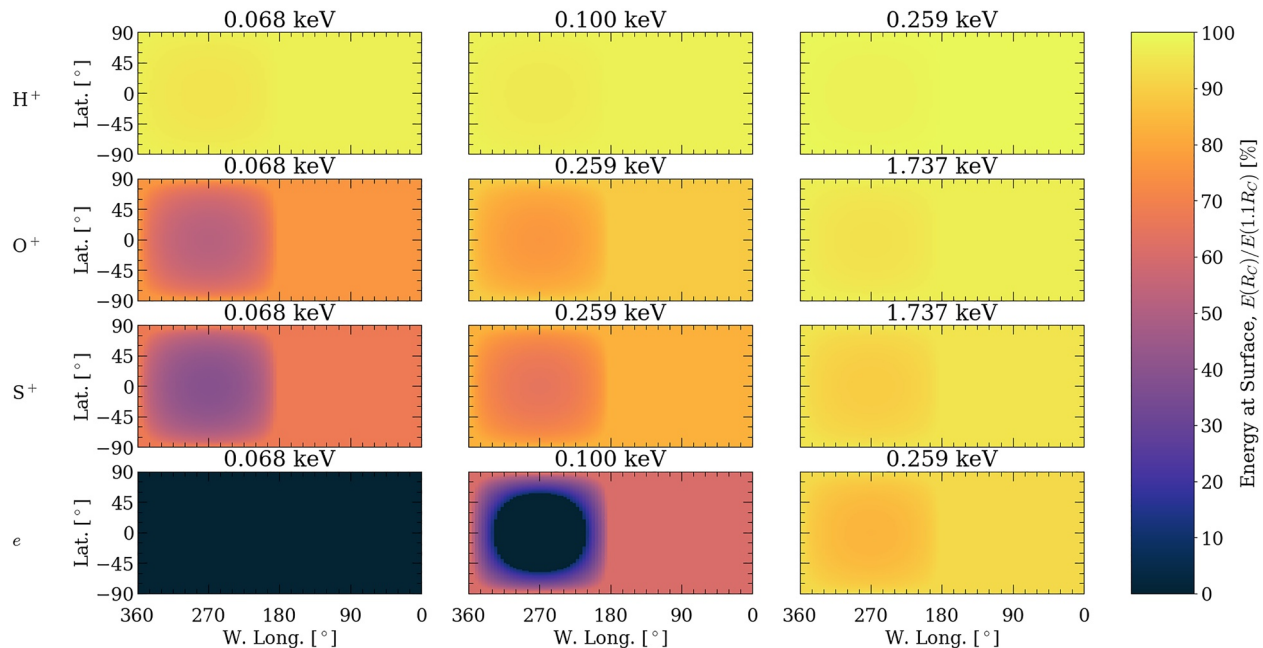


Figure F1. Similar results as those presented in Figure 4 (in some cases different initial energies are presented) but the implemented uniform surface density of the O₂ atmosphere is $n_{0,O_2} = 10^9 \text{ cm}^{-3}$ (rather than $n_{0,O_2} = 10^{10} \text{ cm}^{-3}$).

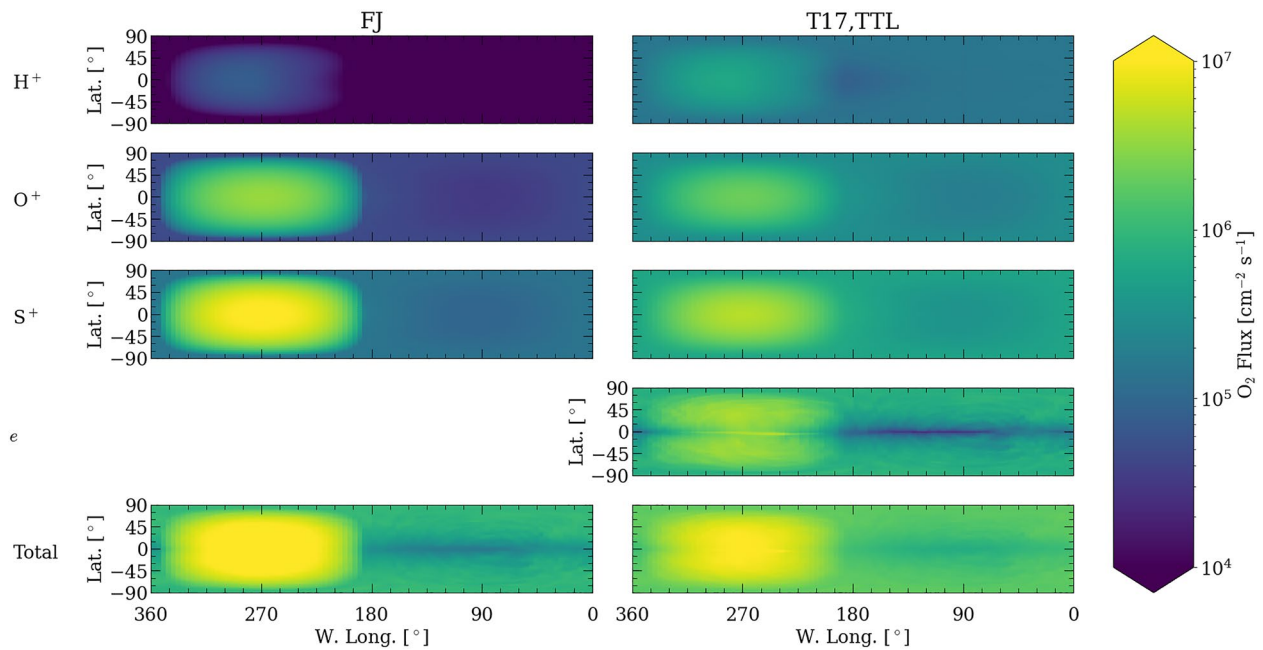


Figure F2. Same results as those presented in Figure 5 but the implemented uniform surface density of the O_2 atmosphere is $n_{0,O_2} = 10^9 \text{ cm}^{-3}$ (rather than $n_{0,O_2} = 10^{10} \text{ cm}^{-3}$).

densities corresponding to the energies of the impinging plasma as well as the total column (integrated across all energies and all plasma components) are illustrated in Figure F3. As can be seen, solving Equation 4 gives $N_{O_2} \sim 3.8 \times 10^{13} \text{ cm}^{-2}$ using the FJ formula and $N_{O_2} \sim 3.1 \times 10^{13} \text{ cm}^{-2}$ using the TTL formula, both of which are $\sim 2\text{--}3$ orders of magnitude less than that inferred from observations, $\sim 4 \times 10^{15} \text{ cm}^{-2}$ (Cunningham et al., 2015; de Kleer et al., 2023)— $\sim 4 \times 10^{16} \text{ cm}^{-2}$ (Kliore et al., 2002).

Table F1

Total Radiolytic Production Rates of O_2 Induced by Energetic H^+ , O^+ , S^+ , and e in an O_2 Atmosphere With an Assumed Surface Density of Density of $n_{0,O_2} = 10^9 \text{ cm}^{-3}$

Plasma	Production rate [$(\times 10^{23}) \text{ s}^{-1}$]		Percentage of total [%]	
	FJ	TTL	FJ	TTL
H^+	0.14	1.6	0.40	6.8
O^+	5.0	4.3	17	18
S^+	16	9.0	54	38
e		8.7 ^a	29	37
Total	30	24	100	

^aThe O_2 production rate induced by energetic electrons is derived via the original formula from Teolis et al. (2017).

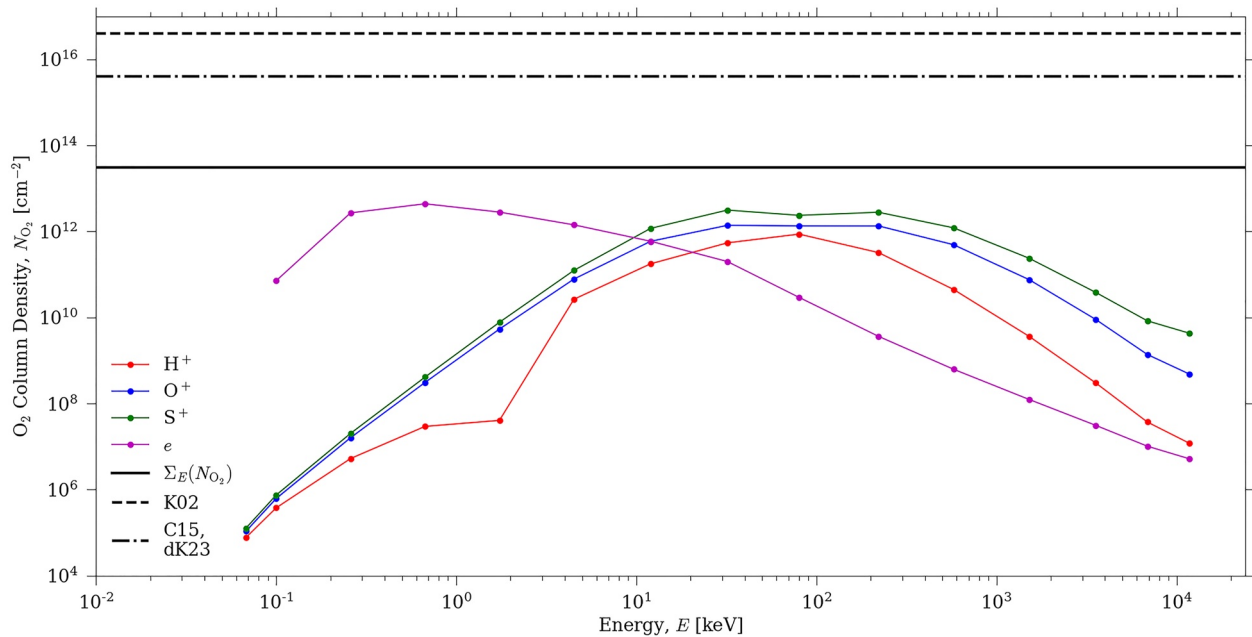


Figure F3. Same results as those presented in Figure 6 but the implemented uniform surface density of the O₂ atmosphere is $n_{0,O_2} = 10^9 \text{ cm}^{-3}$ (rather than $n_{0,O_2} = 10^{10} \text{ cm}^{-3}$).

Data Availability Statement

Results used in this study can be found in Liuzzo (2022) and Carberry Mogan, Liuzzo, et al. (2023).

Acknowledgments

The authors acknowledge support from NASA Solar System Workings Grants 80NSSC21K0152 and 80NSSC22K0097, and New Frontiers Data Analysis Program Grant 80NSSC21K0823.

References

- Addison, P., Liuzzo, L., & Simon, S. (2022). Effect of the magnetospheric plasma interaction and solar illumination on ion sputtering of Europa's surface ice. *Journal of Geophysical Research: Space Physics*, 127(2), e2021JA030136. <https://doi.org/10.1029/2021ja030136>
- Bagenal, F., & Delamere, P. A. (2011). Flow of mass and energy in the magnetospheres of Jupiter and Saturn. *Journal of Geophysical Research*, 116(A5), A05209. <https://doi.org/10.1029/2010ja016294>
- Berger, M. J. (1995). ESTAR, PSTAR and ASTAR: Computer programs for calculating stopping powers and ranges for electrons, protons and helium ions. Technical report.
- Boring, J. W., Johnson, R. E., Reimann, C. T., Garret, J. W., Brown, W. L., & Marcantonio, K. J. (1983). Ion-induced chemistry in condensed gas solids. *Nuclear Instruments and Methods in Physics Research*, 218(1–3), 707–711. [https://doi.org/10.1016/0167-5087\(83\)91070-0](https://doi.org/10.1016/0167-5087(83)91070-0)
- Brown, W. L., Augustyniak, W. M., Marcantonio, K. J., Simmons, E. H., Boring, J. W., Johnson, R. E., & Reimann, C. T. (1984). Electronic sputtering of low temperature molecular solids. *Nuclear Instruments and Methods in Physics Research Section B: Beam Interactions with Materials and Atoms*, 1(2–3), 307–314. [https://doi.org/10.1016/0168-583x\(84\)90085-5](https://doi.org/10.1016/0168-583x(84)90085-5)
- Brown, W. L., Augustyniak, W. M., Simmons, E., Marcantonio, K. J., Lanzerotti, L. J., Johnson, R. E., et al. (1982). Erosion and molecule formation in condensed gas films by electronic energy loss of fast ions. *Nuclear Instruments and Methods in Physics Research*, 198(1), 1–8. [https://doi.org/10.1016/0167-5087\(82\)90043-6](https://doi.org/10.1016/0167-5087(82)90043-6)
- Brown, W. L., Lanzerotti, L. J., Poate, J. M., & Augustyniak, W. M. (1978). Sputtering of ice by MeV light ions. *Physical Review Letters*, 40(15), 1027–1030. <https://doi.org/10.1103/physrevlett.40.1027>
- Calvin, W. M., & Clark, R. N. (1991). Modeling the reflectance spectrum of Callisto 0.25 to 4.1 μm . *Icarus*, 89(2), 305–317. [https://doi.org/10.1016/0019-1035\(91\)90180-2](https://doi.org/10.1016/0019-1035(91)90180-2)
- Carberry Mogan, S. R., Johnson, R. E., Vorburger, A., & Roth, L. (2023). Electron impact ionization in the icy Galilean satellites' atmospheres. *The European Physical Journal D*, 77(2), 1–9. <https://doi.org/10.1140/epjd/s10053-023-00606-8>
- Carberry Mogan, S. R., Liuzzo, L., Poppe, A. R., Simon, S., Szalay, J. R., Tucker, O. J., & Johnson, R. E. (2023). Data for “Callisto's atmosphere: The oxygen enigma” by Carberry Mogan, et al., 2023. <https://doi.org/10.5281/zenodo.7897784>
- Carberry Mogan, S. R., Tucker, O. J., Johnson, R. E., Roth, L., Alday, J., Vorburger, V., et al. (2022). Callisto's atmosphere: First evidence for H₂ and constraints on H₂O. *Journal of Geophysical Research: Planets*, 127(11), e2022JE007294. <https://doi.org/10.1029/2022je007294>
- Carberry Mogan, S. R., Tucker, O. J., Johnson, R. E., Sreenivasan, K. R., & Kumar, S. (2020). The influence of collisions and thermal escape in Callisto's atmosphere. *Icarus*, 352, 113932. <https://doi.org/10.1016/j.icarus.2020.113932>
- Carberry Mogan, S. R., Tucker, O. J., Johnson, R. E., Vorburger, A., Galli, A., Marchand, B., et al. (2021). A tenuous, collisional atmosphere on Callisto. *Icarus*, 368, 114597. <https://doi.org/10.1016/j.icarus.2021.114597>
- Carlson, R. W. (1999). A tenuous carbon dioxide atmosphere on Jupiter's moon Callisto. *Science*, 283(5403), 820–821. <https://doi.org/10.1126/science.283.5403.820>
- Cartwright, R. J., Nordheim, T. A., Cruikshank, D. P., Hand, K. P., Roser, J. E., Grundy, W. M., et al. (2020). Evidence for sulfur-bearing species on Callisto's leading hemisphere: Sourced from Jupiter's irregular satellites or Io? *The Astrophysical Journal Letters*, 902(2), L38. <https://doi.org/10.3847/2041-8213/abbda4>

- Cassidy, T. A., Paranicas, C. P., Shirley, J. H., Dalton, J. B., III., Teolis, B. D., Johnson, R. E., et al. (2013). Magnetospheric ion sputtering and water ice grain size at Europa. *Planetary and Space Science*, 77, 64–73. <https://doi.org/10.1016/j.pss.2012.07.008>
- Clark, R. N. (1980). Ganymede, Europa, Callisto, and Saturn's rings: Compositional analysis from reflectance spectroscopy. *Icarus*, 44(2), 388–409. [https://doi.org/10.1016/0019-1035\(80\)90033-0](https://doi.org/10.1016/0019-1035(80)90033-0)
- Clark, R. N., & McCord, T. B. (1980). The Galilean satellites: New near-infrared spectral reflectance measurements (0.65–2.5 μm) and a 0.325–5 μm summary. *Icarus*, 41(3), 323–339. [https://doi.org/10.1016/0019-1035\(80\)90217-1](https://doi.org/10.1016/0019-1035(80)90217-1)
- Cooper, J. F., Johnson, R. E., Mauk, B. H., Garrett, H. B., & Gehrels, N. (2001). Energetic ion and electron irradiation of the icy Galilean satellites. *Icarus*, 149(1), 133–159. <https://doi.org/10.1006/icar.2000.6498>
- Cosby, P. C. (1993). Electron-impact dissociation of oxygen. *The Journal of Chemical Physics*, 98(12), 9560–9569. <https://doi.org/10.1063/1.464387>
- Cunningham, N. J., Spencer, J. R., Feldman, P. D., Strobel, D. F., France, K., & Osterman, S. N. (2015). Detection of Callisto's oxygen atmosphere with the Hubble space telescope. *Icarus*, 254, 178–189. <https://doi.org/10.1016/j.icarus.2015.03.021>
- Davis, M. R., Meier, R. M., Cooper, J. F., & Loeffler, M. J. (2021). The contribution of electrons to the sputter-produced O₂ exosphere on Europa. *The Astrophysical Journal Letters*, 908(2), L53. <https://doi.org/10.3847/2041-8213/abe415>
- de Kleer, K., Milby, Z., Schmidt, C., Camarca, M., & Brown, M. E. (2023). The optical aurorae of Europa, Ganymede, and Callisto. *The Planetary Science Journal*, 4(2), 37. <https://doi.org/10.3847/psj/acb53c>
- Famá, M., Shi, J., & Baragiola, R. A. (2008). Sputtering of ice by low-energy ions. *Surface Science*, 602(1), 156–161. <https://doi.org/10.1016/j.susc.2007.10.002>
- Frank, L. A., Ackerson, K. L., Wolfe, J. H., & Mihalov, J. D. (1976). Observations of plasmas in the Jovian magnetosphere. *Journal of Geophysical Research*, 81(4), 457–468. <https://doi.org/10.1029/ja081i004p00457>
- Galli, A., Vorburger, A., Wurz, P., Pommerol, A., Cerubini, R., Jost, B., et al. (2018). 0.2 to 10 keV electrons interacting with water ice: Radiolysis, sputtering, and sublimation. *Planetary and Space Science*, 155, 91–98. <https://doi.org/10.1016/j.pss.2017.11.016>
- Garrett, H. B., Jun, I., Ratliff, J., Evans, R., Clough, G., & McEntire, R. (2003). *Galileo interim radiation electron model* (p. 72). The Jet Propulsion Laboratory, California Inst. of Technology, Pasadena, CA Publication 03-006.
- Grundy, W. M., Buie, M. W., Stansberry, J. A., Spencer, J. R., & Schmitt, B. (1999). Near-infrared spectra of icy outer solar system surfaces: Remote determination of H₂O ice temperatures. *Icarus*, 142(2), 536–549. <https://doi.org/10.1006/icar.1999.6216>
- Gurnett, D. A., Kurth, W. S., Roux, A., & Bolton, S. J. (1997). Absence of a magnetic-field signature in plasma-wave observations at Callisto. *Nature*, 387(6630), 261–262. <https://doi.org/10.1038/387261a0>
- Gurnett, D. A., Persoon, A. M., Kurth, W. S., Roux, A., & Bolton, S. J. (2000). Plasma densities in the vicinity of Callisto from Galileo plasma wave observations. *Geophysical Research Letters*, 27(13), 1867–1870. <https://doi.org/10.1029/2000gl003751>
- Hall, D. T., Strobel, D. F., Feldman, P. D., McGrath, M. A., & Weaver, H. A. (1995). Detection of an oxygen atmosphere on Jupiter's moon Europa. *Nature*, 373(6516), 677–679. <https://doi.org/10.1038/373677a0>
- Hartkorn, O., Saur, J., & Strobel, D. F. (2017). Structure and density of Callisto's atmosphere from a fluid-kinetic model of its ionosphere: Comparison with Hubble Space Telescope and Galileo observations. *Icarus*, 282, 237–259. <https://doi.org/10.1016/j.icarus.2016.09.020>
- Hendrix, A. R., & Johnson, R. E. (2008). Callisto: New insights from Galileo disk-resolved UV measurements. *The Astrophysical Journal*, 687(1), 706–713. <https://doi.org/10.1086/591491>
- Huebner, W. F., & Mukherjee, J. (2015). Photoionization and photodissociation rates in solar and blackbody radiation fields. *Planetary and Space Science*, 106, 11–45. <https://doi.org/10.1016/j.pss.2014.11.022>
- Johnson, R. E. (1990). *Energetic charged-particle interactions with atmospheres and surfaces*. Springer Science & Business Media.
- Johnson, R. E., Boring, J. W., Reimann, C. T., Barton, L. A., Sieveka, E. M., Garrett, J. W., et al. (1983). Plasma ion-induced molecular ejection on the Galilean satellites: Energies of ejected molecules. *Geophysical Research Letters*, 10(9), 892–895. <https://doi.org/10.1029/gl1010i009p00892>
- Johnson, R. E., Burger, M. H., Cassidy, T. A., Leblanc, F., Marconi, M., & Smyth, W. H. (2009). *Composition and detection of Europa's sputter-induced atmosphere* (pp. 507–527). Europa, University of Arizona Press.
- Johnson, R. E., Carlson, R. W., Cooper, J. F., Paranicas, C., Moore, M. H., & Wong, M. C. (2004). Radiation effects on the surfaces of the Galilean satellites. In *Jupiter: The planet, satellites and magnetosphere* (pp. 485–512).
- Johnson, R. E., & Jesser, W. A. (1997). O₂/O₃ microatmospheres in the surface of Ganymede. *The Astrophysical Journal Letters*, 480(1), L79–L82. <https://doi.org/10.1086/310614>
- Johnson, R. E., Oza, A. V., Leblanc, F., Schmidt, C., Nordheim, T. A., & Cassidy, T. A. (2019). The origin and fate of O₂ in Europa's ice: An atmospheric perspective. *Space Science Reviews*, 215(1), 20. <https://doi.org/10.1007/s11214-019-0582-1>
- Jun, I., Garrett, H. B., Cassidy, T. A., Kim, W., & Dougherty, L. (2019). Updating the Jovian electron plasma environment. *IEEE Transactions on Plasma Science*, 47(8), 3915–3922. <https://doi.org/10.1109/tps.2019.2901681>
- Kim, T. K., Ebert, R. W., Valek, P. W., Allegrini, F., McComas, D. J., Bagenal, F., et al. (2020). Survey of ion properties in Jupiter's plasma sheet: Juno JADE-I observations. *Journal of Geophysical Research: Space Physics*, 125(4), e2019JA027696. <https://doi.org/10.1029/2019ja027696>
- Kivelson, M. G., Bagenal, F., Kurth, W. S., Neubauer, F. M., Paranicas, C., & Saur, J. (2004). Magnetospheric interactions with satellites. In *Jupiter: The planet, satellites and magnetosphere* (pp. 513–536).
- Kliore, A. J., Anabtawi, A., Herrera, R. G., Asmar, S. W., Nagy, A. F., Hinson, D. P., & Flasar, F. M. (2002). Ionosphere of Callisto from Galileo radio occultation observations. *Journal of Geophysical Research*, 107(A11), 1407. SIA–19. <https://doi.org/10.1029/2002ja009365>
- Lanzerotti, L. J., Brown, W. L., Poate, J. M., & Augustyniak, W. M. (1978). On the contribution of water products from Galilean satellites to the Jovian magnetosphere. *Geophysical Research Letters*, 5(2), 155–158. <https://doi.org/10.1029/jg005i002p00155>
- Leblanc, F., Oza, A. V., Leclercq, L., Schmidt, C., Cassidy, T., Modolo, R., et al. (2017). On the orbital variability of Ganymede's atmosphere. *Icarus*, 293, 185–198. <https://doi.org/10.1016/j.icarus.2017.04.025>
- Liang, M.-C., Lane, B. F., Pappalardo, R. T., Allen, M., & Yung, Y. L. (2005). Atmosphere of Callisto. *Journal of Geophysical Research*, 110(E2), E02003. <https://doi.org/10.1029/2004je002322>
- Liuzzo, L. (2022). Data for “Energetic Particle Fluxes onto Callisto's Atmosphere” by Liuzzo et al., 2022. <https://doi.org/10.5281/zenodo.6784734>
- Liuzzo, L., Feyerabend, M., Simon, S., & Motschmann, U. (2015). The impact of Callisto's atmosphere on its plasma interaction with the Jovian magnetosphere. *Journal of Geophysical Research: Space Physics*, 120(11), 9401–9427. <https://doi.org/10.1002/2015ja021792>
- Liuzzo, L., Poppe, A. R., Addison, P., Simon, S., Nénon, Q., & Paranicas, C. (2022). Energetic magnetospheric particle fluxes onto Callisto's atmosphere. *Journal of Geophysical Research: Space Physics*, 127(11), e2022JA030915. <https://doi.org/10.1029/2022ja030915>
- Liuzzo, L., Simon, S., & Feyerabend, M. (2018). Observability of Callisto's inductive signature during the Jupiter icy moons explorer mission. *Journal of Geophysical Research: Space Physics*, 123(11), 9045–9054. <https://doi.org/10.1029/2018ja025951>
- Liuzzo, L., Simon, S., Feyerabend, M., & Motschmann, U. (2016). Disentangling plasma interaction and induction signatures at Callisto: The Galileo C10 flyby. *Journal of Geophysical Research: Space Physics*, 121(9), 8677–8694. <https://doi.org/10.1002/2016ja023236>

- Liuzzo, L., Simon, S., Feyeraend, M., & Motschmann, U. (2017). Magnetic signatures of plasma interaction and induction at Callisto: The Galileo C21, C22, C23, and C30 flybys. *Journal of Geophysical Research: Space Physics*, *122*(7), 7364–7386. <https://doi.org/10.1002/2017ja024303>
- Liuzzo, L., Simon, S., & Regoli, L. (2019a). Energetic electron dynamics near Callisto. *Planetary and Space Science*.
- Liuzzo, L., Simon, S., & Regoli, L. (2019b). Energetic ion dynamics near Callisto. *Planetary and Space Science*, *166*, 23–53. <https://doi.org/10.1016/j.pss.2018.07.014>
- Luspay-Kuti, A., Mousis, O., Lunine, J. I., Ellinger, Y., Pauzat, F., Raut, U., et al. (2018). Origin of molecular oxygen in comets: Current knowledge and perspectives. *Space Science Reviews*, *214*(8), 1–24. <https://doi.org/10.1007/s11214-018-0541-2>
- Luspay-Kuti, A., Mousis, O., Pauzat, F., Ozgurel, O., Ellinger, Y., Lunine, J. I., et al. (2022). Dual storage and release of molecular oxygen in comet 67P/Churyumov–Gerasimenko. *Nature Astronomy*, *6*(6), 724–730. <https://doi.org/10.1038/s41550-022-01614-1>
- Mandeville, J.-C., Geake, J. E., & Dollfus, A. (1980). Reflectance polarimetry of Callisto and the evolution of the Galilean satellites. *Icarus*, *41*(3), 343–355. [https://doi.org/10.1016/0019-1035\(80\)90219-5](https://doi.org/10.1016/0019-1035(80)90219-5)
- Mauk, B., Haggerty, D., Jaskulek, S., Schlemm, C., Brown, L., Cooper, S., et al. (2017). The Jupiter energetic particle detector instrument (JEDI) investigation for the Juno mission. *Space Science Reviews*, *213*(1–4), 289–346. <https://doi.org/10.1007/s11214-013-0025-3>
- Mauk, B., Mitchell, D., McEntire, R., Paranicas, C., Roelof, E., Williams, D., et al. (2004). Energetic ion characteristics and neutral gas interactions in Jupiter's magnetosphere. *Journal of Geophysical Research*, *109*(A9), A09S12. <https://doi.org/10.1029/2003ja010270>
- McComas, D., Alexander, N., Allegrini, F., Bagenal, F., Beebe, C., Clark, G., et al. (2017). The Jovian auroral distributions experiment (JADE) on the Juno mission to Jupiter. *Space Science Reviews*, *213*(1–4), 547–643. <https://doi.org/10.1007/s11214-013-9990-9>
- McCord, T. B., Carlson, R. W., Smythe, W. D., Hansen, G. B., Clark, R. N., Hibbitts, C. A., et al. (1997). Organics and other molecules in the surfaces of Callisto and Ganymede. *Science*, *278*(5336), 271–275. <https://doi.org/10.1126/science.278.5336.271>
- McCord, T. B., Hansen, G. B., Clark, R. N., Martin, P. D., Hibbitts, C. A., Fanale, F. P., et al. (1998). Non-water-ice constituents in the surface material of the icy Galilean satellites from the Galileo near-infrared mapping spectrometer investigation. *Journal of Geophysical Research*, *103*(E4), 8603–8626. <https://doi.org/10.1029/98je00788>
- Meier, R. M., & Loeffler, M. J. (2020). Sputtering of water ice by keV electrons at 60 K. *Surface Science*, *691*, 121509. <https://doi.org/10.1016/j.susc.2019.121509>
- Moore, J. M., Asphaug, E., Morrison, D., Spencer, J. R., Chapman, C. R., Bierhaus, B., et al. (1999). Mass movement and landform degradation on the icy Galilean satellites: Results of the Galileo nominal mission. *Icarus*, *140*(2), 294–312. <https://doi.org/10.1006/icar.1999.6132>
- Moore, J. M., Chapman, C. R., Bierhaus, E. B., Greeley, R., Chuang, F. C., Klemaszewski, J., et al. (2004). Callisto. Jupiter: The planet, satellites and magnetosphere (Vol. 1, pp. 397–426).
- Morrison, D., & Cruikshank, D. P. (1973). Thermal properties of the Galilean satellites. *Icarus*, *18*(2), 224–236. [https://doi.org/10.1016/0019-1035\(73\)90207-8](https://doi.org/10.1016/0019-1035(73)90207-8)
- Mousis, O., Ronnet, T., Brugger, B., Ozgurel, O., Pauzat, F., Ellinger, Y., et al. (2016). Origin of molecular oxygen in comet 67P/Churyumov–Gerasimenko. *The Astrophysical Journal Letters*, *823*(2), L41. <https://doi.org/10.3847/2041-8205/823/2/L41>
- Müller, J., Simon, S., Motschmann, U., Schüle, J., Glassmeier, K.-H., & Pringle, G. J. (2011). Aikef: Adaptive hybrid model for space plasma simulations. *Computer Physics Communications*, *182*(4), 946–966. <https://doi.org/10.1016/j.cpc.2010.12.033>
- Orlando, T. M., & Sieger, M. T. (2003). The role of electron-stimulated production of O₂ from water ice in the radiation processing of outer solar system surfaces. *Surface Science*, *528*(1–3), 1–7. [https://doi.org/10.1016/s0039-6028\(02\)02602-x](https://doi.org/10.1016/s0039-6028(02)02602-x)
- Paranicas, C., Hibbitts, C. A., Kollmann, P., Ligier, N., Hendrix, A. R., Nordheim, T. A., et al. (2018). Magnetospheric considerations for solar system ice state. *Icarus*, *302*, 560–564. <https://doi.org/10.1016/j.icarus.2017.12.013>
- Pilcher, C. B., Ridgway, S. T., & McCord, T. B. (1972). Galilean satellites: Identification of water frost. *Science*, *178*(4065), 1087–1089. <https://doi.org/10.1126/science.178.4065.1087>
- Reimann, C. T., Boring, J. W., Johnson, R. E., Garrett, J. W., Farmer, K. R., Brown, W. L., et al. (1984). Ion-induced molecular ejection from D2O ice. *Surface Science*, *147*(1), 227–240. [https://doi.org/10.1016/0039-6028\(84\)90177-8](https://doi.org/10.1016/0039-6028(84)90177-8)
- Roth, L., Alday, J., Becker, T. M., Ivchenko, N., & Retherford, K. D. (2017). Detection of a hydrogen corona at Callisto. *Journal of Geophysical Research: Planets*, *122*(5), 1046–1055. <https://doi.org/10.1002/2017je005294>
- Roush, T. L., Pollack, J. B., Witteborn, F. C., Bregman, J. D., & Simpson, J. P. (1990). Ice and minerals on Callisto: A reassessment of the reflectance spectra. *Icarus*, *86*(2), 355–382. [https://doi.org/10.1016/0019-1035\(90\)90225-x](https://doi.org/10.1016/0019-1035(90)90225-x)
- Saur, J., Grambusch, T., Duling, S., Neubauer, F., & Simon, S. (2013). Magnetic energy fluxes in sub-Alfvénic planet star and moon planet interactions. *Astronomy & Astrophysics*, *552*, A119. <https://doi.org/10.1051/0004-6361/201118179>
- Saur, J., Neubauer, F. M., Strobel, D. F., & Summers, M. E. (1999). Three-dimensional plasma simulation of Io's interaction with the Io plasma torus: Asymmetric plasma flow. *Journal of Geophysical Research*, *104*(A11), 25105–25126. <https://doi.org/10.1029/1999ja003034>
- Scarlett, L. H., Tapley, J. K., Fursa, D. V., Zammit, M. C., Savage, J. S., & Bray, I. (2018). Electron-impact dissociation of molecular hydrogen into neutral fragments. *The European Physical Journal D*, *72*(2), 1–8. <https://doi.org/10.1140/epjdd/2017-80649-8>
- Schenk, P. M. (1995). The geology of Callisto. *Journal of Geophysical Research*, *100*(E9), 19023–19040. <https://doi.org/10.1029/95je01855>
- Shematovich, V., & Johnson, R. (2001). Near-surface oxygen atmosphere at Europa. *Advances in Space Research*, *27*(11), 1881–1888. [https://doi.org/10.1016/s0273-1177\(01\)00299-x](https://doi.org/10.1016/s0273-1177(01)00299-x)
- Shematovich, V. I. (2006). Stochastic models of hot planetary and satellite coronas: Atomic oxygen in Europa's corona. *Solar System Research*, *40*(3), 175–190. <https://doi.org/10.1134/s0038094606030014>
- Shematovich, V. I., Johnson, R. E., Cooper, J. F., & Wong, M. C. (2005). Surface-bounded atmosphere of Europa. *Icarus*, *173*(2), 480–498. <https://doi.org/10.1016/j.icarus.2004.08.013>
- Smith, E. J., Davis, L., Jr., Jones, D. E., Coleman, P. J., Jr., Colburn, D. S., Dyal, P., et al. (1974). The planetary magnetic field and magnetosphere of Jupiter: Pioneer 10. *Journal of Geophysical Research*, *79*(25), 3501–3513. <https://doi.org/10.1029/ja079i025p03501>
- Spencer, J. R. (1987a). Icy Galilean satellite reflectance spectra: Less ice on Ganymede and Callisto? *Icarus*, *70*(1), 99–110. [https://doi.org/10.1016/0019-1035\(87\)90077-7](https://doi.org/10.1016/0019-1035(87)90077-7)
- Spencer, J. R. (1987b). Thermal segregation of water ice on the Galilean satellites. *Icarus*, *69*(2), 297–313. [https://doi.org/10.1016/0019-1035\(87\)90107-2](https://doi.org/10.1016/0019-1035(87)90107-2)
- Spencer, J. R. (1987c). The surface of Europa, Ganymede, and Callisto: An investigation using Voyager IRIS thermal infrared spectra. Doctoral dissertation. The University of Arizona. Retrieved from <https://repository.arizona.edu/handle/10150/184098>
- Spencer, J. R., & Calvin, W. M. (2002). Condensed O₂ on Europa and Callisto. *The Astronomical Journal*, *124*(6), 3400–3403. <https://doi.org/10.1086/344307>
- Spencer, J. R., & Maloney, P. R. (1984). Mobility of water ice on Callisto: Evidence and implications. *Geophysical Research Letters*, *11*(12), 1223–1226. <https://doi.org/10.1029/g1011i012p01223>

- Squyres, S. W. (1980). Surface temperatures and retention of H₂O frost on Ganymede and Callisto. *Icarus*, *44*(2), 502–510. [https://doi.org/10.1016/0019-1035\(80\)90040-8](https://doi.org/10.1016/0019-1035(80)90040-8)
- Stern, S. A., Cook, J. C., Chaufray, J.-Y., Feldman, P. D., Gladstone, G. R., & Retherford, K. D. (2013). Lunar atmospheric H₂ detections by the lamp UV spectrograph on the lunar reconnaissance orbiter. *Icarus*, *226*(2), 1210–1213. <https://doi.org/10.1016/j.icarus.2013.07.011>
- Strobel, D. F., Saur, J., Feldman, P. D., & McGrath, M. A. (2002). Hubble space telescope space telescope imaging spectrograph search for an atmosphere on Callisto: A Jovian unipolar inductor. *The Astrophysical Journal Letters*, *581*(1), L51–L54. <https://doi.org/10.1086/345803>
- Teolis, B. D., Plainaki, C., Cassidy, T. A., & Raut, U. (2017). Water ice radiolytic O₂, H₂, and H₂O₂ yields for any projectile species, energy, or temperature: A model for icy astrophysical bodies. *Journal of Geophysical Research: Planets*, *122*(10), 1996–2012. <https://doi.org/10.1002/2017je005285>
- Tribbett, P. D., & Loeffler, M. J. (2021). The sputtering of radiolytic O₂ in ion irradiated H₂O-ice. *Surface Science*, *707*, 121797. <https://doi.org/10.1016/j.susc.2021.121797>
- Tucker, O. J., Farrell, W. M., Killen, R. M., & Hurley, D. M. (2019). Solar wind implantation into the lunar regolith: Monte Carlo simulations of H retention in a surface with defects and the H₂ exosphere. *Journal of Geophysical Research: Planets*, *124*(2), 278–293. <https://doi.org/10.1029/2018je005805>
- Vorburger, A., Pflieger, M., Lindkvist, J., Holmström, M., Lammer, H., Lichtenegger, H. I. M., et al. (2019). 3D-modeling of Callisto's surface sputtered exosphere environment. *Journal of Geophysical Research: Space Physics*, *124*(8), 7157–7169. <https://doi.org/10.1029/2019ja026610>
- Vorburger, A., Wurz, P., Lammer, H., Barabash, S., & Mousis, O. (2015). Monte-Carlo simulation of Callisto's exosphere. *Icarus*, *262*, 14–29. <https://doi.org/10.1016/j.icarus.2015.07.035>
- Walker, A. C., Moore, C. H., Goldstein, D. B., Varghese, P. L., & Trafton, L. M. (2012). A parametric study of Io's thermophysical surface properties and subsequent numerical atmospheric simulations based on the best fit parameters. *Icarus*, *220*(1), 225–253. <https://doi.org/10.1016/j.icarus.2012.05.001>
- Wilson, R. (2022). Jade standard product data record and archive volume software interface specification. <https://doi.org/10.17189/1519715>
- Wolfe, J. H., Collard, H., Mihalov, J., & Intriligator, D. (1974). Preliminary Pioneer 10 encounter results from the Ames Research Center plasma analyzer experiment. *Science*, *183*(4122), 303–305. <https://doi.org/10.1126/science.183.4122.303>
- Wurz, P., Abplanalp, D., Tulej, M., & Lammer, H. (2012). A neutral gas mass spectrometer for the investigation of lunar volatiles. *Planetary and Space Science*, *74*(1), 264–269. <https://doi.org/10.1016/j.pss.2012.05.016>
- Yung, Y. L., & McElroy, M. B. (1977). Stability of an oxygen atmosphere on Ganymede. *Icarus*, *30*(1), 97–103. [https://doi.org/10.1016/0019-1035\(77\)90124-5](https://doi.org/10.1016/0019-1035(77)90124-5)
- Ziegler, J. F., & Biersack, J. P. (1985). The stopping and range of ions in matter. In *Treatise on heavy-ion science* (pp. 93–129). Springer.